Bulletin of the Seismological Society of America, Vol. 106, No. 2, pp. –, April 2016, doi: 10.1785/0120140250

Ⓔ

A Fault-Based Model for Crustal Deformation, Fault Slip Rates, and Off-Fault Strain Rate in California

by Yuehua Zeng and Zheng-Kang Shen

Abstract We invert Global Positioning System (GPS) velocity data to estimate fault slip rates in California using a fault-based crustal deformation model with geologic constraints. The model assumes buried elastic dislocations across the region using Uniform California Earthquake Rupture Forecast Version 3 (UCERF3) fault geometries. New GPS velocity and geologic slip-rate data were compiled by the UCERF3 deformation working group. The result of least-squares inversion shows that the San Andreas fault slips at 19–22 mm/yr along Santa Cruz to the North Coast, 25–28 mm/yr along the central California creeping segment to the Carrizo Plain, 20–22 mm/yr along the Mojave, and 20–24 mm/yr along the Coachella to the Imperial Valley. Modeled slip rates are 7–16 mm/yr lower than the preferred geologic rates from the central California creeping section to the San Bernardino North section. For the Bartlett Springs section, fault slip rates of 7–9 mm/yr fall within the geologic bounds but are twice the preferred geologic rates. For the central and eastern Garlock, inverted slip rates of 7.5 and 4.9 mm/yr, respectively, match closely with the geologic rates. For the western Garlock, however, our result suggests a low slip rate of 1.7 mm/yr. Along the eastern California shear zone and southern Walker Lane, our model shows a cumulative slip rate of 6.2–6.9 mm/yr across its east–west transects, which is ~1 mm/yr increase of the geologic estimates. For the off-coast faults of central California, from Hosgri to San Gregorio, fault slips are modeled at 1–5 mm/yr, similar to the lower geologic bounds. For the off-fault deformation, the total moment rate amounts to 0.88×10^{19} N·m/yr, with fast straining regions found around the Mendocino triple junction, Transverse Ranges and Garlock fault zones, Landers and Brawley seismic zones, and farther south. The overall California moment rate is 2.76×10^{19} N·m/yr, which is a 16% increase compared with the UCERF2 model.

Online Material: Table of geological slip rates.

Introduction

The National Seismic Hazard Maps are constructed principally using three types of data that constrain the rate of activity on faults: instrumental seismicity data, paleoseismic observations on past earthquake occurrence, and geodetic constraints on fault slip rates and strain accumulation rates (Petersen *et al.*, 2014). Although the first and second data sets define the rate, style, and location of past earthquake activity, the third data set defines crustal deformation that may potentially lead to future earthquakes.

In the U.S. Geological Survey (USGS)/Southern California Earthquake Center Uniform California Earthquake Rupture Forecast Version 2 (UCERF2) deformation models, fault slip rates were assigned based on an expert-opinion evaluation of available geologic and geodetic data and were constrained by the total plate rate. Figure 1a shows the Global Positioning System (GPS) velocity distribution of the California Crustal Motion Map v.1.0 (Shen *et al.*, 2006) from the Working Group on California Earthquake Probabilities project. Based on the preferred UCERF2.1 deformation model (Field *et al.*, 2009), we predicted the velocities at the same GPS sites and plotted the residual velocities, computed as the difference between the observed GPS velocities and those predicted by the UCERF2.1 model. Residuals are large and systematic, particularly in the Transverse Ranges, Mojave Desert, the eastern California shear zone, near Parkfield, and the San Francisco Bay area, implying that UCERF2 models

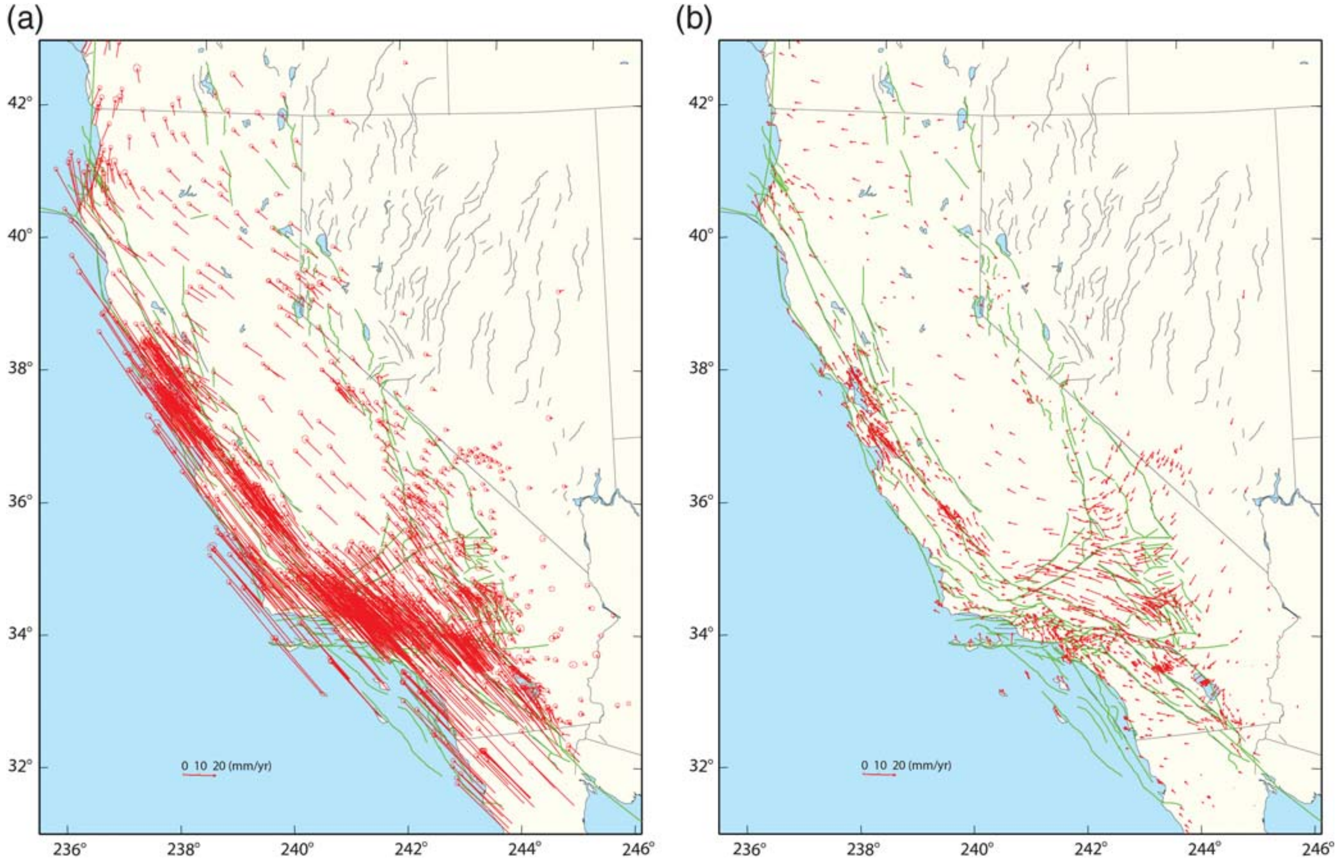

Figure 1. (a) Global Positioning System (GPS) velocity vectors for California and its neighbors from the California Crustal Motion Map v.1.0 (Shen *et al.*, 2006), referenced to the North American plate. (b) Residual velocities computed as the difference between the observed GPS velocities and those predicted using the Uniform California Earthquake Rupture Forecast Version 2.1 (UCERF2.1) deformation model. The velocity scales in (a) and (b) are the same. The residual vectors imply that UCERF2 generally underestimates the average statewide deformation rate, although we do not know how much of the actual deformation is aseismic. The green lines are the modeled fault traces, and gray lines are the remaining Basin and Ranges faults.

generally underestimate the average statewide deformation rate.

The discrepancy described above calls for the development of a systematic procedure that uses all available data to better estimate on-fault slip rates and off-fault deformation rates. A viable approach is to use a deformation model that is well constrained by both GPS and geologic data. Previous deformation models apply either block-like models (e.g., d'Alessio *et al.*, 2005; McCaffrey, 2005; Meade and Hagar, 2005) or non-block-like models (Johnson *et al.*, 2007; Pollitz and Schwartz, 2008; Bird, 2009; Chuang and Johnson, 2011; Hearn *et al.*, 2013; Zeng and Shen, 2014) and have been successful in providing insight into the broad tectonic deformation and estimates of fault slip rates. For most cases, the geodetic and geologic slip-rate estimates agree. For some faults, however, large discrepancies exist between the two different estimates, such as along the San Bernardino Mountain and Mojave segments of the San Andreas fault (McCaffrey, 2005; Meade and Hagar, 2005). Now, under the UCERF3 project, a new compilation of geologic and geodetic data is available, providing a unique opportunity to revisit the existing models and to develop new approaches that better estimate on-fault slip rates and gridded off-fault deformation covering all of California.

This article describes the development of a fault-based crustal deformation model for California using the kinematic fault model of Zeng and Shen (2014). Updated GPS velocities and geological slip rates for the UCERF3 project are used as model constraints. Major blocks and their boundaries are constructed by linking all the major California fault segments (or type A faults) except the Garlock fault. All other minor faults (or type B faults) distributed in the block interiors are modeled as buried dislocation sources (Savage and Burford, 1973). Type A faults in California are faults that have slip rates greater than 5 mm/yr and sufficient paleoseismic data to constrain fault behavior (Petersen *et al.*, 1996; Field *et al.*, 2009). Other significant California faults are categorized as type B faults, with measurable slip rates but inadequate paleoseismic data to constrain the recurrence intervals of large events. Geologic data that constrain slip-rate estimates at point locations on faults were compiled by Dawson and Weldon (2013) for the UCERF3 project. Geologic bounds from Dawson and Weldon (2013) are also available to constrain slip rates on non-block boundary faults (type B faults). Two sets of models have been developed under the UCERF3 project: a block-like model and a fault-based model. This article focuses on the result of the fault-based deformation model for California. Our fault-based model provides direct slip-rate estimates on the UCERF3 faults. In the off-coast area and along the eastern California shear zone where geologic measurements are lacking, this study provides the necessary constraints on fault slip-rate estimates. The results also provide gridded off-fault strain rates to compare with other seismic-hazard inputs, for example, the Gutenberg–Richter a-value distribution based on seismicity, regional strain mechanisms as determined from earthquake moment tensors and focal mechanisms, and earthquake moment budget from other studies. Final slip rates from this mode have been applied to UCERF3 as the preferred model for California seismic-hazard analysis.

Method

Zeng and Shen (2014) developed a kinematic fault network model that simulates ground deformation rates from a given distribution of slip rates across all the faults in a region. For a given slip-rate and creep-rate distribution on all the faults, the ground velocity vector at any point is obtained by taking a sum of multiplication of the static finite-fault Green's function with the uniform slip rate over the faults:

$$\dot{u}_n(\mathbf{r}_i) = \sum_{j=1}^{N}(\mathrm{U}^1_{nj}\Delta\dot{u}^j_1 + \mathrm{U}^2_{nj}\Delta\dot{u}^j_2) + \sum_{k=1}^{M}(\mathrm{U}^1_{\mathrm{creep},nk}\Delta c^k_1 + \mathrm{U}^2_{\mathrm{creep},nk}\Delta c^k_2), \quad (1)$$

in which $\dot{u}_n$ is the predicted surface velocities; n is the component of the horizontal velocities; $\mathbf{r}_i$ is the location of the ith station; $\Delta\dot{u}^j_1$ and $\Delta\dot{u}^j_2$ are the fault-parallel and fault-normal slip rates along the jth fault segment, respectively; U^1_{nj} and U^2_{nj} are the Green's function relating those fault slip rates to velocities at the ith station; Δc^k_1 and Δc^k_2 are the fault-parallel and fault-normal creep rate along the kth fault segment, respectively; $\mathrm{U}^1_{\mathrm{creep},nk}$ and $\mathrm{U}^2_{\mathrm{creep},nk}$ are the Green's function relating the fault creep rates at shallow depth to velocities at the ith station; N is the total number of fault segments; and M is the total number of creeping fault segments.

Our kinematic fault model assumes that each fault segment slips at a certain rate beneath a locking depth, except for a few fault segments where shallow creep is allowed. We also impose slip vector continuity at fault nodes or intersections to regulate slip variability and to simulate block-like motion. In addition, we minimize slip rates along the fault-normal direction because fault systems in the region are dominated by strike-slip faults. This minimization is intended to balance motion along fault-normal and fault-parallel directions. In places where primary slip is found to be fault-normal, our test suggests the effect is rather insignificant at around 2% reduction in normal slip-rate estimation when data are sufficient. Together with equation (1), they form the basis for solving for slip-rate distribution using a least-squares inversion. An increase in the weighting of the continuity constraint will result in a more block-like deformation model; in contrast, loose continuity constraints result in a fault-patch-only deformation model. The degree of weighting on the continuity constraint is optimally selected from a trade-off curve between the data postfit residual chi-squares and the parameter resolution of the model, so that certain non-block-like deformation features are allowed, such as deformation caused by permanent or transient strain build-up within the bounding blocks.

Other distributed type B faults are modeled as buried dislocations using equation (1). Locking depths in general could also be optimized based on the goodness-of-fit between model prediction and geodetic observations. Instead, for the type A faults, fault-locking depth is determined based on seismicity depth distribution along faults available in the literature (e.g., Hill *et al.*, 1990; Hauksson, 2000). For the rest, fault-locking depth is fixed to the values specified by the UCERF3.1 fault model. We use the Okada (1985) formulation and code to calculate surface deformation in an elastic half-space. This could be a problem at the large plate boundary scale when using a half-space model to approximate a spherical Earth (Sun *et al.*, 2009). However, Banerjee *et al.* (2005) found that the agreement between a spherical homogeneous Earth and a half-space calculation is within a few percent within an ~5° distance, and the difference only grows quickly beyond 10° distance. Because our California model covers mostly a region of 5° × 10°, we would expect a few percent bias by the half-space approximation.

In addition to the on-fault slip rate, we calculate the off-fault strain rates. The calculation brings deeply buried dislocation sources up to the surface along the boundaries of all the major blocks and computes strain-rate tensors on a gridded zone covering California, assuming the same slip-rate distribution along their surface fault segments as that along their buried dislocation sections. Given a strict block-like model, we would expect zero off-fault strain rates. However, for a general non-block-like model, we find nontrivial strain-rate distribution left in the block interiors after all block boundary faults break to the surface. Thus our off-fault strain rates are the result of strain accumulation due to non-block-like faulting along the block boundaries as those faults break to the surface. The release of those strains correlates with the off-fault seismicity. Other off-fault sources, such as faults that are not included in our current model and distributed permanent strains, should also contribute to the off-fault strains and be included in our future improvement. Both on-fault and off-fault inversion rates may include a significant aseismic component, and further study is needed to separate it from the total inversion rates for seismic-hazard evaluation. Slip-rate parameters developed from this article are intended for alternative models for the 2014 seismic-hazard evaluation for California and its surrounding area.

Fault Model

One of the key components of UCERF3 is the fault model project led by Dawson (2013) to update the UCERF2 fault models. The update includes a few central-coast faults and improved Great Valley faults. Major changes are made to the fault representations for northern California. For southern California, the model is similar to that of the UCERF2 fault models. This new UCERF3.1 model has been used as the basis for fault-based and block deformation models. In the process of building a block model, faults are connected to form blocks. For major faults, block boundaries follow their traces almost exactly. For small faults, they are generalized into a single representation as part of bigger block boundaries. Efforts were taken to correct any distortion of the earlier block boundary geometry that resulted in GPS stations located on the wrong side of the fault, for example near the Parkfield and Carrizo Plain sections of the San Andreas fault.

For our fault-based model, we connected the type A faults (except the Garlock fault) to form several major blocks and distributed other type B faults in the interior of those blocks, with the same geometries provided by the UCERF3.1 fault model, including dip and locking depths. The Garlock fault was assumed to be a large buried crack that branched out of the San Andreas fault. We also added a few Nevada faults near the Reno–Carson area. Figure 2 shows the locations of faults in our fault-based model (red and white traces). The six major blocks include the Pacific block (blue), North American block (gray), Juan de Fuca block (cyan), San Jacinto block (red), Maacama–Hayward block (yellow), and Bartlett Springs–Green Valley block (purple). We imposed slip vector continuity conditions for the major blocks bounded by the type A faults (thick red in Fig. 2) in the region so the enclosed zones by those faults will behave in a more block-like fashion. In addition, we also added a southern branch to extend the San Andreas fault system into Mexico and northern branches to extend the Mendocino fault farther east and the Cascadia subduction zone north of the triple junction. These additions extend well outside the model domain to allow us to model the far-field relative motions between the North American plate and the Pacific plate due to buried dislocations.

We included shallow creep in some of the fault segments, for example, along the central California creeping segment, the Calaveras, Hayward, and Imperial Valley faults, and the Brawley seismic zone. We also allow partial locking for the northern Parkfield and southern Santa Cruz Mountain segments of the San Andreas fault zone. Creep is assumed to occur at a constant rate from the surface to 10 km depth for most creeping faults except the central California creeping section and the Brawley seismic zone. For the central California creeping section, we assume depth-dependent creep rates from the surface to 5 km depth and from 5 km to deep down in the Earth with uniform rate in each depth range, respectively. The creeping depth along the Brawley seismic zone is set to be equal to its locking depth because of its shallow seismogenic layer. The amount of creep along those creeping segments is determined from inversion of the GPS observations.

GPS Data

The GPS velocity field used for this study was constructed by Tom Herring for the UCERF3 project (Parsons *et al.*, 2013). This is consensus data averaged from several data processing groups. Some uncertainties in the field are as low as 0.1 mm/yr. Our test inversions found that using these very small uncertainties could overweight their corresponding observations. Therefore, we imposed a lower cutoff of 0.2 mm/yr to avoid over-weighting during the inversions. The velocity field was further edited by Rob McCaffrey based on visual inspection of the velocities on their consistency with neighbors. To avoid the edits being model dependent, data being removed were those for which the velocities are not consistent with neighbors, at the 3–4 mm/yr level differences, and are not near faults. Some USGS campaign GPS data near the Yucca Mountain region have rates that are different from the azimuth of the rates from the continuous stations in the area. The difference might be introduced by a difference in reference frame. The sites were removed. We also removed data with sigma larger than 1.0 mm/yr.

Figure 3 shows a map view of the GPS velocity field. A sharp gradient in GPS velocities is shown across the entire San Andreas fault system, the eastern California shear zone, and along the Walker Lane near the California and Nevada border. The GPS velocities are similar across the Sierra Nevada/Great Valley block, suggesting near-rigid behavior of the block.

Geologic Constraints

Dawson and Weldon (2013) compiled geologic slip rates for faults in the UCERF3 fault model. Instead of the expert opinion or consensus slip rates adopted by UCERF2, this compilation is intended to be a purely geologic estimate of late Quaternary slip rates at locations along faults within the UCERF3 fault model. In general, slip rates were compiled from the literature with good location information and reliable dating of offset features. This compilation does not include slip rates that (1) rely on assumptions of characteristic slip, (2) are heavily model dependent (such as using ratio assumptions to derive horizontal slip rates from amounts of vertical offset), or (3) may need revision due to revised dating at a site. In addition, rates that are somewhat suspect, because they may be derived from features offset by a small number of earthquakes that may not represent a long term average, are also excluded. A single representative slip rate or averaged slip rate is reported for any location.

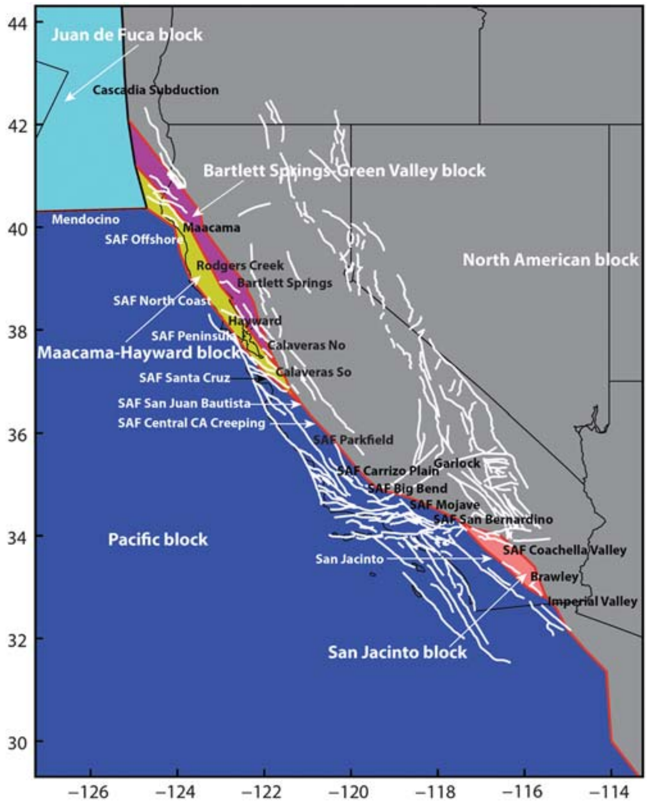

Figure 2. Major blocks: Pacific block (blue), North American block (gray), Juan de Fuca block (cyan), San Jacinto block (red), Maacama–Hayward block (yellow), and Bartlett Springs–Green Valley block (purple). Those California type A faults are connected to form block boundaries (red lines) The UCERF3.1 type B faults are distributed among the blocks (white lines).

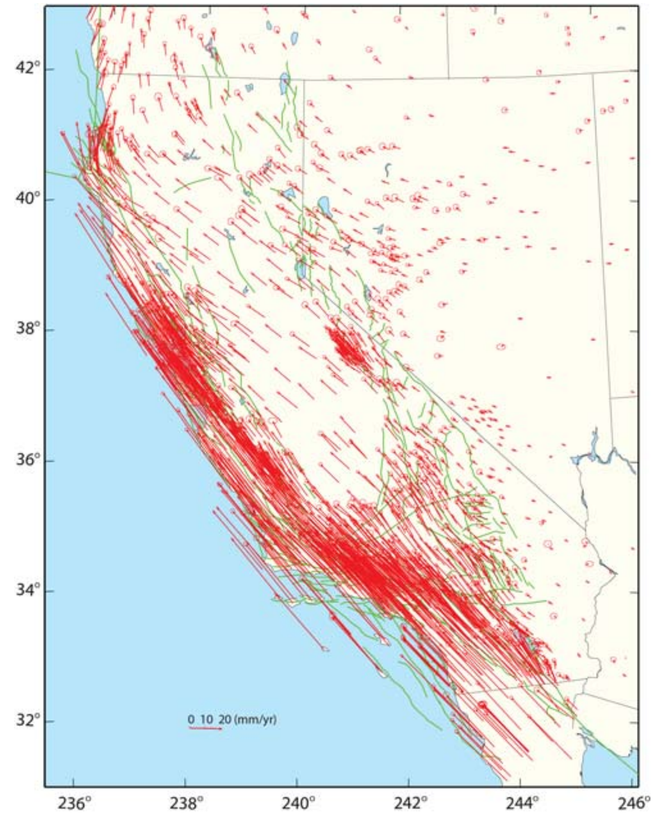

Figure 3. Distribution of UCERF3 GPS velocity vectors for California and its neighbors, referenced to the North American plate. Error ellipses represent 50% confidence. The green lines are the modeled fault traces.

For this model, we use either the preferred rates or averages of the minimum and maximum values as our geologic constraints with their corresponding uncertainties. For some sites, uncertainties are not available. We compute a linear regression between slip rates and their uncertainty estimates and assign the predicted uncertainties from this regression to the rates at those sites. We only considered sites that are located along the UCERF3.1 fault traces. Figure 4 plots the geologic sites used for the fault-based model. Ⓔ A list of all the geologic slip rates used in this study, together with their corresponding site locations, faulting style, and standard errors, is provided in the electronic supplement to this article.

Fault rake and slip-rate bounds are also provided by Dawson and Weldon (2013) for the UCERF3 fault model. This information was derived mostly from the slip-rate category assigned to faults in the USGS Quaternary Fault and Fold Database (see Data and Resources). A few rates are based on geologic knowledge for specific faults with slip rates less than 5 mm/yr. This information was optional for modelers and was provided to constrain any nonsensical results (e.g., right-lateral faults slipping in a left-lateral sense). Rakes are used as input constraints for type B faults in our least-squares inversion with ±20° tolerance for reverse/normal and strike-slip faults, and ±30° for oblique faults. For type A faults, rake angles were well defined and were all fixed to pure strike-slip faulting. In addition, we increased weights on the geologic constraints of those faults until their slip rates fell within their estimated geologic bounds for either type B faults or all California faults. Although our final preferred model is the B fault bound model, we will show the all-fault bound model result to support our preferred choice.

Results and Discussion

Following the inversion method of Zeng and Shen (2014), we compute inverse solutions for the fault-based model. We use the same weighting parameters for the slip-rate vector continuity constraints across fault-node points and for minimizing slip rate along fault-normal components as in Zeng and Shen (2014). In addition to the geologic constraints on slip rates at locations where geologic estimates are available, we assign a 50 mm/yr constraint on slip rate at the extended southern end of the San Andreas fault zone to simulate the relative plate motion between the Pacific and the North American plates based on the NUVEL-1A model (DeMets *et al.*, 1994), a 35 mm/yr slip rate to the Mendocino fault and its west extension based on the UCERF3.1 geologic model, and a 28 mm/yr constraint on locking rate to the

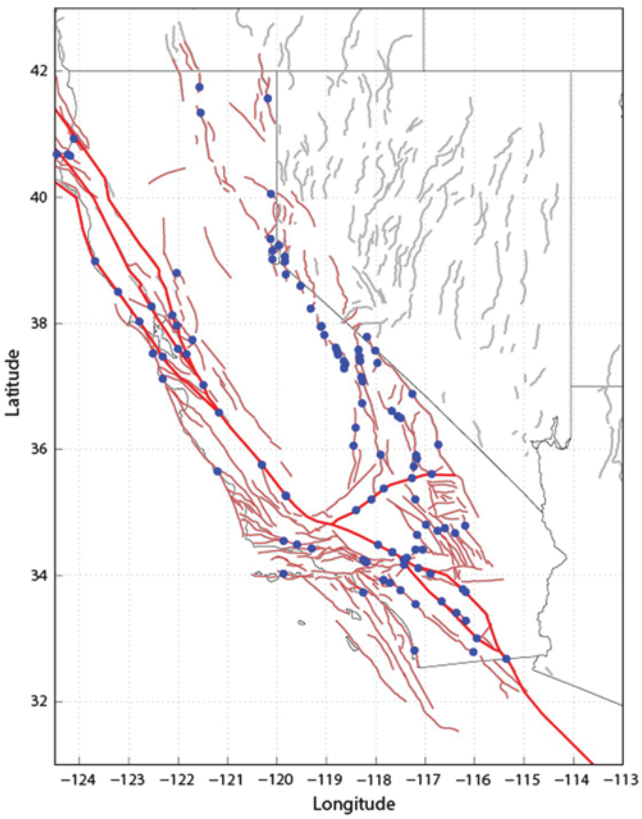

Figure 4. Geologic sites (blue solid circles) used for the fault-based model and the location of UCERF3.1 faults in California (red lines).

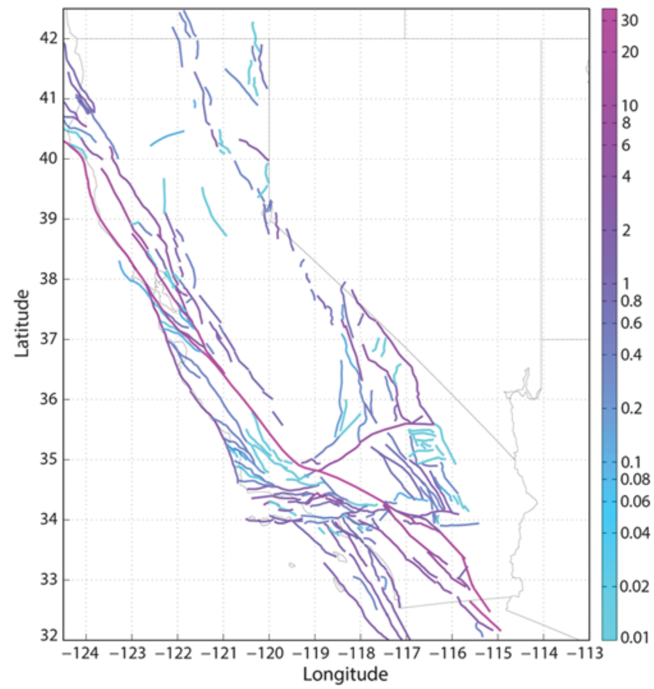

Figure 5. California fault traces, color-coded based on the magnitude of the estimated fault slip rates on all type A and B faults from the preferred inversion model. Units in the color bar are millimeters per year.

southern Cascadia subduction zone based also on the NUVEL-1A model.

Modeling Statistics and General Slip-Rate Comparison

Figure 5 shows the estimated slip rates on all California type A and B faults, color-coded based on the magnitude of the estimated fault slip rates from our preferred inversion model. The range of slip rates is distributed from high-slip-rate type A faults to low-slip-rate type B faults. Figure 6a compares observed GPS velocities (red) with the model predicted GPS velocities (blue) based on a combined GPS and geologic slip-rate inversion using the fault-based crustal deformation model. Figure 6b shows the residual GPS velocities. Those residuals are given by the differences between the observed velocities and those predicted by the preferred final inverse model with a mean residual of 1.6 mm/yr and a normalized chi-square error of 15.1.

We test a case without the geologic constraints, and its normalized chi-square error is reduced to 9.9 with a mean residual of 1.3 mm/yr. By honoring the geologic constraints as required by the UCERF3 project, we compromised the GPS fit by 23% in terms of mean residual and increased the normalized chi-square error by 50%. The normalized chi-square error also depends on the selected lower cutoff uncertainties to the GPS observation. The reported uncertainties in the velocity field are as small as 0.1 mm/yr. Our test inversions find that those small uncertainties overwhelm the corresponding observations and produce an unstable inverse solution. A lower cutoff of 0.2 mm/yr was used to avoid excessive over-weighting during the inversions. Without re-running the inversion, a slightly higher cutoff of 0.3 mm/yr reduces our normalized chi-square error to 10.7. This higher cutoff value was tested in geodesy- and geology-based slip-rate model inversions for the western United States National Seismic Hazard Maps (Petersen *et al.*, 2013) and the UCERF3 NeoKinema model (Parsons *et al.*, 2013). It has resulted in significantly lower chi-square errors, for instance in the UCERF3 NeoKinema model.

Misfit distribution is spatially uneven, with notably large misfits (> 2 mm/yr) in the area near the Landers and Hector Mine earthquakes, which probably represents inadequate corrections for postseismic deformation in the region (Liu *et al.*, 2015). Large misfits near the Long Valley caldera are partly caused by the Long Valley volcanism, which is not included in our model. Large misfits in the populated areas of southern California and San Francisco Bay area are likely influenced by human activities, such as underground water extraction. There are still small trends in the residuals, such as in the Mojave and near Long Valley caldera, where unmodeled tectonic features contributed to the bias. The model accommodates all major features observed in the GPS velocity field, for example, the sharp gradient in GPS velocity amplitudes across the San Andreas fault system, the eastern

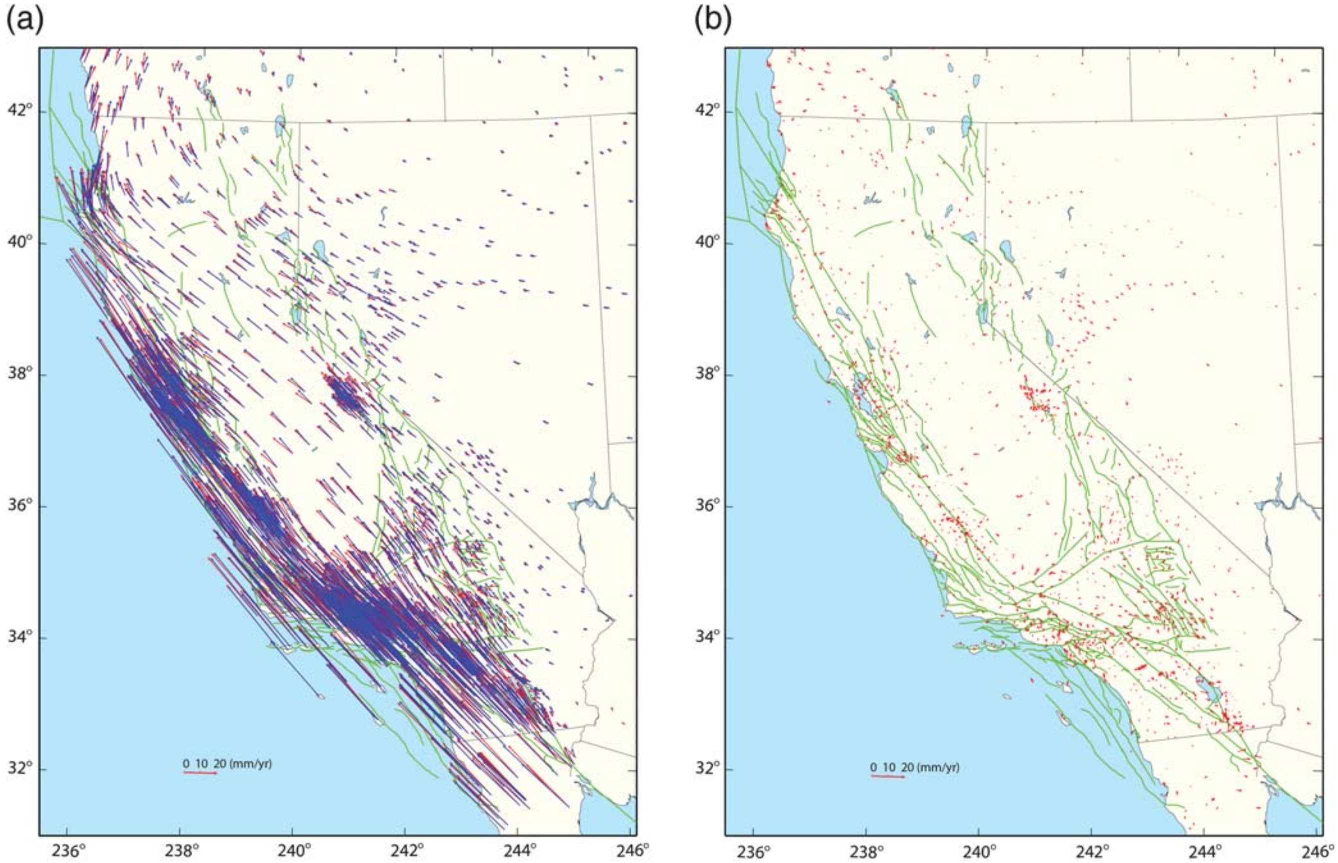

Figure 6. (a) Comparison between observed (red) and inversion prediction (blue) of GPS velocity vectors for California and its neighbors, referenced to the North American plate. (b) Residual velocities for inversion using the fault-based model with geologic constraints. The residual velocities are given by the difference between the observed GPS velocities and the predicted GPS velocities computed using the preferred inversion model. The green lines are the modeled fault traces. The residual vectors are plotted in the same scale as the GPS velocities in (a).

California shear zone, and along the Walker Lane near the California and Nevada border, the near-constant velocity across the Sierra Nevada/Great Valley block, and the rotation of the velocity field north of the Mendocino triple junction. In comparison with Figure 1b, the current model, based on combined inversion of geodetic and geologic data, constitutes a significant improvement in GPS velocity residual reduction compared with the UCERF2 models based on expert opinions for many geologic fault slip rates.

The discrepancy between geologic and geodetic estimates of fault slip rates provides insight into the complex interactions in the system and the extent of incompleteness of our deformation model. Figure 7 plots the slip rates from the fault-based model inversion against the measured geologic slip rates (Dawson and Weldon, 2013). Although the modeled slip rates are obtained from inversions with the geologic constraints, differences among the two rates reflect the difference between contemporary geodetic deformations and long-term geologic ground movements. Modeled slip rates are higher than geologic slip rates mostly on faults in the eastern California shear zone and southern Walker Lane. Modeled rates are lower than geologic slip rates mostly along the central and southern San Andreas fault zone, particularly along the Mojave and San Bernardino Mountain segments. The modeled rate is low along the western Garlock fault. Despite the differences, the modeled slip rates correlate well with the geologic estimates, with a correlation coefficient of 0.9. Statistically this shows a strong linear dependence between the model estimates and the geologic estimates, suggesting that the geodetic and geologic data are highly compatible for the region. Figure 7 also indicates that the correlation line between the geologic and modeled rates has a slope less than one, suggesting that geologic rates are systematically faster than geodetic rates, in particular along the central California creeping section through the Mojave to the San Bernardino Mountain segments of the San Andreas.

Figure 8 compares modeled slip rates with the UCERF3 geologic preferred rates along the California type A faults. We use the geologic upper and lower bounds to represent ranges of the geologic slip-rate uncertainties in the horizontal bars. Vertical bars are inverted slip-rate uncertainties. A solid line indicates where the two rates are equal. Similar to Figure 7, we find the lower inverted slip rates along the Mojave and San Bernardino Mountain segments (upper right

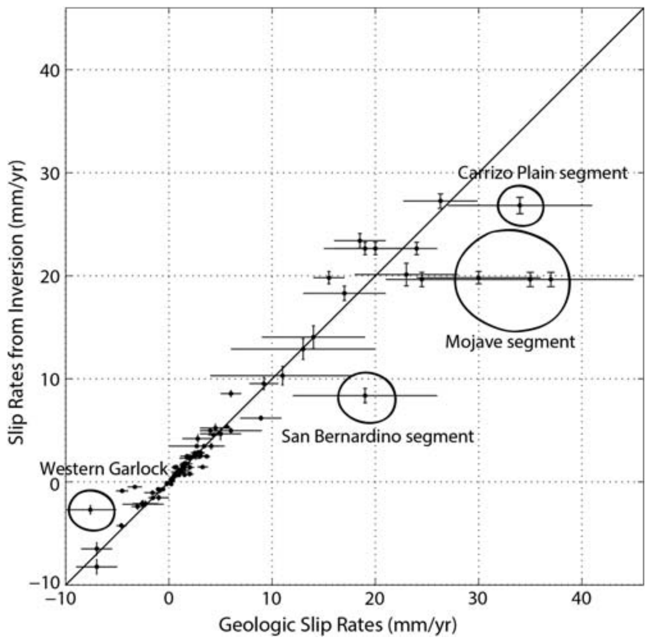

Figure 7. Inverted versus geologic slip rates for California faults. The inverted slip rates are calculated based on inversion with the fault-based model and geologic slip-rate constraints. This model is the preferred inversion model with additional B fault upper and lower geologic bound constraints. The geologic slip rates are from the Dawson and Weldon (2013) slip-rate data based on direct geologic observations. The negative slip rate corresponds to left-lateral/normal slip rate and positive slip rate corresponds to right-lateral/thrust slip rate. Vertical bars are inversion slip-rate uncertainties. The solid line indicates where the two rates are equal. Horizontal bars represent geologic uncertainties.

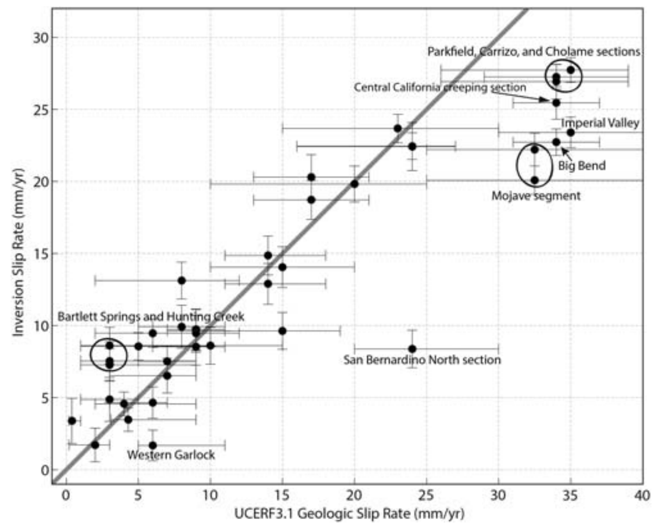

Figure 8. Comparison of preferred inversion slip rates and preferred geologic slip rates along California type A faults. Vertical bars are inversion slip-rate uncertainties. The solid line indicates where the two rates are equal. Horizontal bars represent geologic upper and lower bounds of the geologic preferred slip rates. Circles highlight the slip rates for the faults labeled next to them.

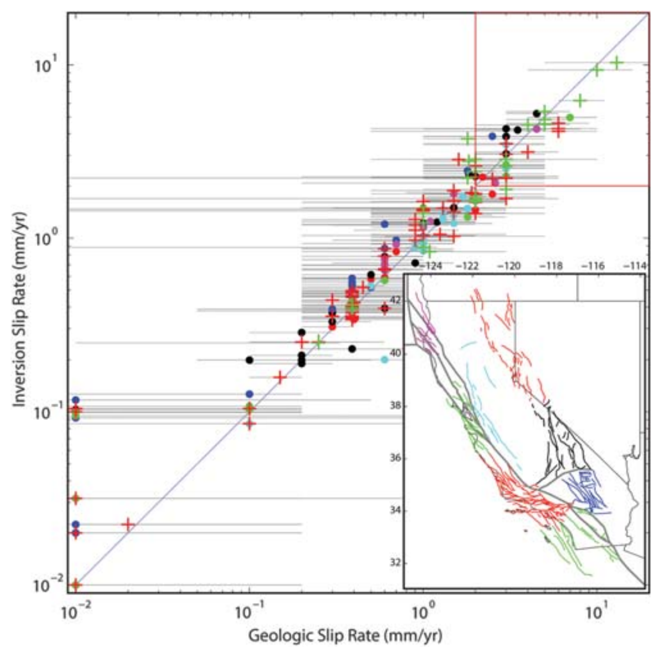

Figure 9. Comparison between the preferred inversion slip rates and preferred geologic slip rates along California type B faults. Horizontal bars represent geologic upper and lower bounds of the geologic preferred slip rates. Color-coded symbols represent faults plotted in the same color code in the lower right panel. The red and green crosses are for faults in southern California, and the solid circles are for the remaining California faults.

corner of Fig. 8) and higher inverted slip rates along the Bartlett Springs and Hunting Creek faults (lower left corner of Fig. 8) in comparison with the geologic rate. The geologic preferred rate for both the Imperial Valley and the Cerro Prieto fault is about 35 mm/yr. Given that there is significant spatial overlap between the two faults, the sum of the two slip rates along the overlapping segments exceeds the relative plate motion between the North American and the Pacific plates. A linear tapering was applied to the faults where overlap occurs to comply with the plate rates (Field *et al.*, 2014). Figure 8 compares the inverted rates and the geologic rates before tapering is applied to the geologic rates. After tapering, the two rates should agree well.

Figure 9 compares inverted slip rates with the geologic preferred rates along all the California type B faults using a logarithmic scale. Again, horizontal bars represent upper and lower bounds of the preferred geologic slip rates. Colored symbols represent faults plotted in the same color in the lower right panel. The red and green crosses are for faults in southern California, and the solid circles are for the rest of the California faults. All the estimates for type B faults fall within the geologic bounds, which is a consequence of the additional geologic bound constraints for these faults. The difference in terms of GPS data fitting between models with and without the additional constraint is nevertheless less than 2%. However, for some of the off-coast faults (red crosses and green solid circles in Fig. 9) and eastern California shear zone faults (dark blue solid circles) with categorical slip-rate

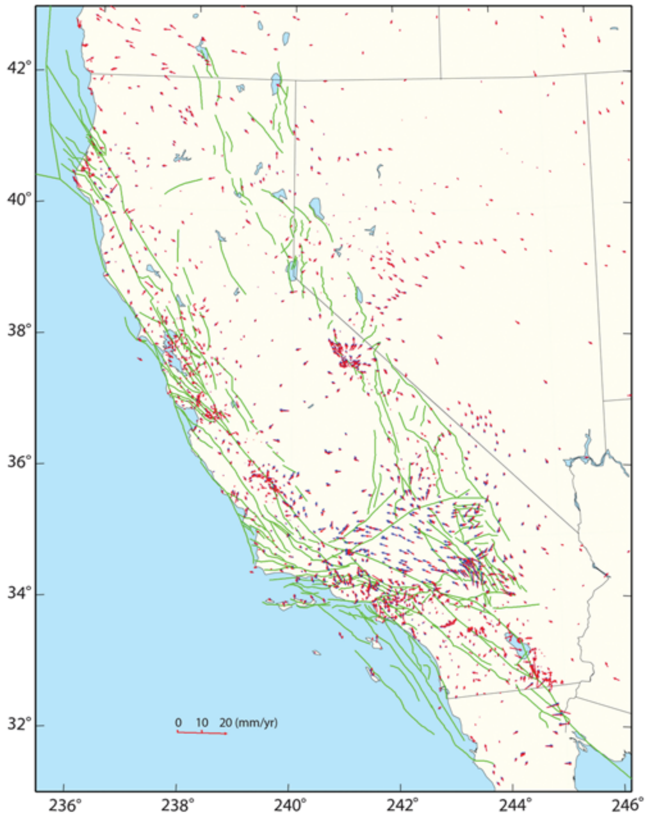

Figure 10. Comparison between GPS residual velocity field based on the preferred inversion model (red; the model with additional slip rates constrained within their geologic bound for all type B faults) and that based on the inversion model with slip rates constrained within geological bounds for all faults (blue). The scale of the residual velocities is twice that plotted in Figure 6b.

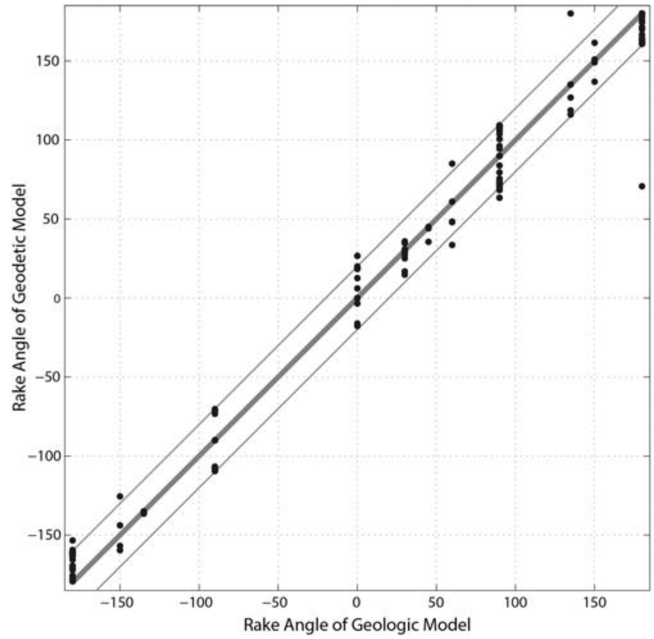

Figure 11. Geodetic versus geologic rake angles for all type B faults. The central black line indicates where the two rakes are equal. The thin lines depart from the unity line at ±20°.

assignment of 0.01 mm/yr, this combined inversion spreads those rates from 0.01 to 0.1 mm/yr, as demanded by the GPS observation. For slip rates > 2 mm/yr (the red square outlining the upper right corner of the plot), the inversion finds lower rates for some of the Transverse Range faults (red crosses) and off-coast faults in southern California (green crosses), and higher rates for some of the eastern California shear zone (dark blue solid circles) and southern Walker Lane (black solid circles) faults in comparison with the geologic preferred rates on those same faults.

Our preferred inversion model is the model constrained to have slip rates within geologic bounds for all type B faults. Questions arise as to how large the GPS data residual misfits becomes if all faults, or just all type B faults, are constrained to have slip rates within geologic bounds. To further explore trade-offs between fitting geodetic and geologic data, we compute inversion with all slip rates held within the geologic bounds except for the Cerro Prieto and Imperial segments, because the best-fit GPS rates for those two faults are in better agreement with the overall plate rate budget. A variable rate was assumed for the central California creeping section. The average rate for the creeping section is within the provided geologic bounds. The bounds on the San Jacinto stepovers were set between 11.0 and 18.0 mm/yr to maintain consistency with the overall San Jacinto geologic bound model. Figure 10 shows a comparison between GPS residual velocity field based on the preferred inversion model (red; with additional slip-rate constraints within their geologic bound for all type B faults) and that based on the inversion model with slip-rate constraints within geological bounds for all faults (blue). For clarity, we enlarged the scale of the residual velocities to twice that plotted in Figure 6b. By carefully examining the spatial residual velocity distribution between the all-fault bound model (blue) and only type B fault bound model (red), we find significant increases in residual velocities in the Mojave Desert and Transverse Ranges and in regions along the Garlock fault zone for the all-fault bound model. The apparent increases in residual velocities are a direct consequence of constraining slip rates within their geologic bounds along the western Garlock and along the Mojave and San Bernardino Mountain segment of the San Andreas fault. The normalized chi-square error for the all-fault bound model is 18.40 and the mean residual is 1.7 mm/yr, a more than 20% significant increase in chi-square errors and a slight increase in the mean residual velocity compared to that of the type B fault bound model.

In addition to the above-mentioned geologic slip-rate constraints, we also imposed rake angle constraints on slip-rate vector solutions for all type B faults using the Dawson and Weldon (2013) geological rake model to avoid rake reversals. This is achieved using a non-negative least squares inversion. Figure 11 compares inverted rake angles with those from the geologic model. The thicker line is where two rakes are equal. The thin lines are ±20° from the unity

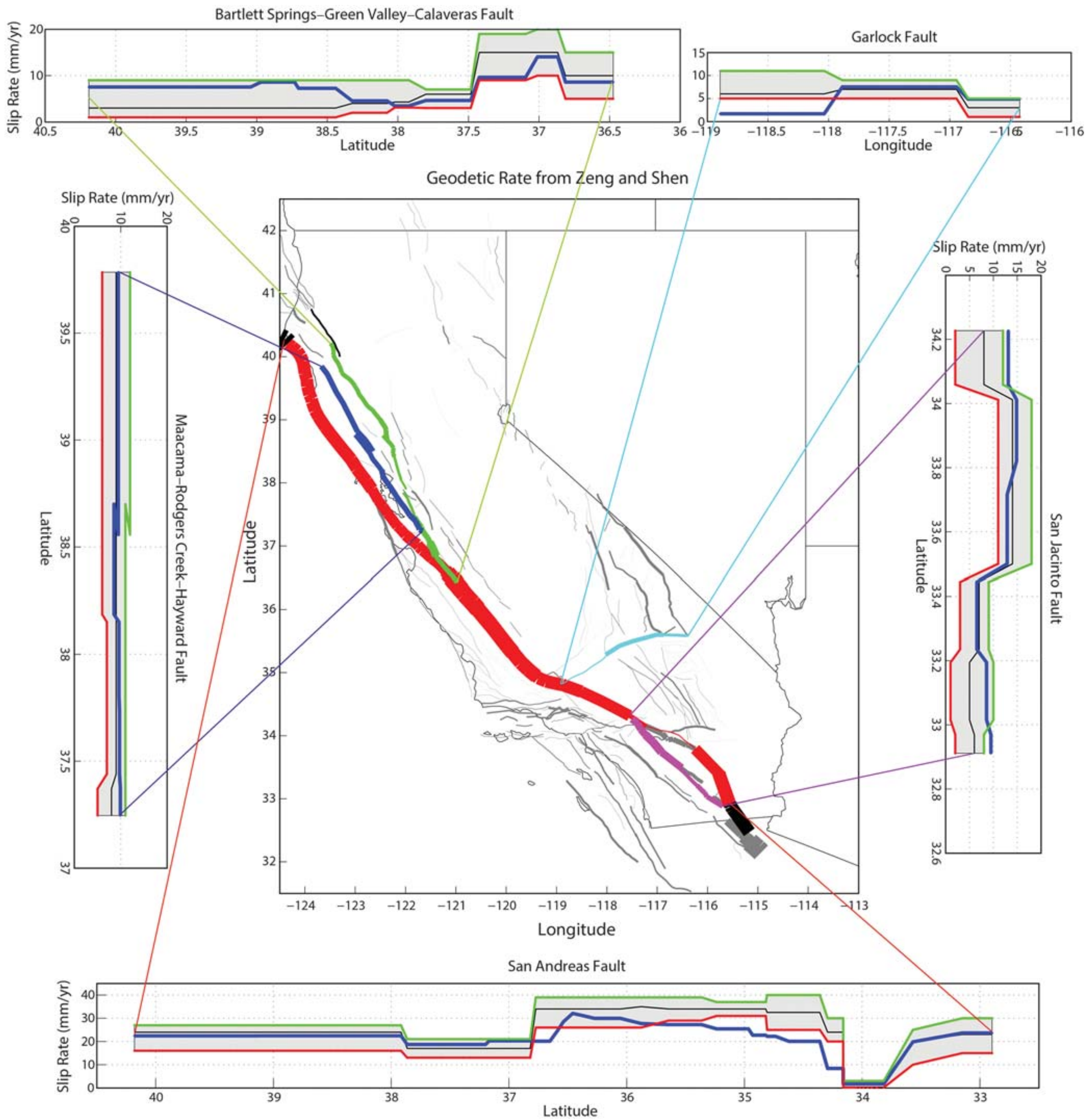

Figure 12. The strike-slip rates determined from inversion with the fault-based model and geologic constraints. The width of the fault traces is proportional to the amount of inverted slip-rate along the corresponding fault segment. Each panel around the map plots the comparison between the geologic preferred slip rates (black) and the geodetic inverted slip rate (blue). The areas between the upper (green) and lower (red) geologic bounds are shaded in gray.

line. For most fault segments, the inverted rake angles are within ±20° bounds of those geologic rakes.

Regional and Fault-by-Fault Slip-Rate Comparisons

In the following discussion, we will focus on fault-by-fault slip-rate comparisons on some major faults between our preferred inversion model with slip rates constrained within geologic bounds for type B faults and the UCERF3.1 geologic model. The central panel of Figure 12 plots a map view of the strike-slip rates along type A faults from the preferred inversion model. The width of the fault traces is proportional to the amount of inverted slip-rate along the corresponding fault segment. Panels around the map show comparisons

Table 1
Slip Rates along the San Andreas Fault Zone Using the Fault-Based Model

Fault Name	Geologic Slip Rate (mm/yr)	Lower Bound (mm/yr)	Upper Bound (mm/yr)	Inverted Slip Rate ± Error (mm/yr)
San Andreas (offshore)	24.0	16.0	27.0	22.42 ± 1.4
San Andreas (North Coast)	24.0	16.0	27.0	22.45 ± 0.6
San Andreas (peninsula)	17.0	13.0	21.0	18.72 ± 0.8
San Andreas (Santa Cruz Mountains)	17.0	13.0	21.0	20.30 ± 1.2
San Andreas (creeping section)	34.0	26.0	39.0	26.92 ± 0.9
San Andreas (Parkfield)	35.0	26.0	39.0	27.73 ± 0.7
San Andreas (Cholame)	34.0	29.0	39.0	27.25 ± 0.7
San Andreas (Carrizo)	34.0	31.0	37.0	25.45 ± 0.8
San Andreas (Big Bend)	34.0	31.0	37.0	22.72 ± 0.6
San Andreas (Mojave North)	32.5	25.0	40.0	22.21 ± 0.7
San Andreas (Mojave South)	32.5	25.0	40.0	20.08 ± 0.7
San Andreas (San Bernardino North)	24.0	20.0	30.0	8.37 ± 0.7
San Andreas (San Bernardino South)	13.00	5.0	20.0	10.31 ± 0.9
San Andreas (north branch Mill Creek)	2.0	0.2	3.0	1.71 ± 0.6
San Andreas (San Gorgonio Pass–Garnet Hill)	10.0	4.0	16.0	9.35 ± 0.9
San Andreas (Coachella)	20.0	10.0	25.0	19.82 ± 0.6
Brawley (seismic zone)	23.0	15.0	30.0	23.67 ± 0.7
Imperial Valley	35.0	30.0	40.0	23.40 ± 0.7
Cerro Prieto	35.0	30.0	40.0	24.15 ± 0.9

Table 2
Slip Rates along the Maacama–Rodgers Creek–Hayward Fault Zone Using the Fault-Based Model

Fault Name	Geologic Slip Rate (mm/yr)	Lower Bound (mm/yr)	Upper Bound (mm/yr)	Inverted Slip Rate ± Error (mm/yr)
Maacama	9.0	6.0	12.0	9.47 ± 0.7
Rodgers Creek–Healdsburg	9.0	6.0	11.0	8.53 ± 0.8
Hayward (North)	9.0	7.0	11.0	9.62 ± 1.0
Hayward (South)	9.0	7.0	11.0	9.73 ± 0.9
Hayward (South) extension	8.0	5.0	11.0	9.92 ± 1.0

Table 3
Slip Rates along Bartlett Springs–Green Valley–Calaveras Fault Segments Using the Fault-Based Model

Fault Name	Geologic Slip Rate (mm/yr)	Lower Bound (mm/yr)	Upper Bound (mm/yr)	Inverted Slip Rate ± Error (mm/yr)
Eaton Roughs	0.39	0.2	1.0	3.38 ± 1.2
Bartlett Springs	3.0	1.0	9.0	7.54 ± 0.9
Hunting Creek–Bartlett Springs connector	3.0	1.0	9.0	8.61 ± 0.9
Hunting Creek–Berryessa	3.0	1.0	9.0	7.27 ± 0.8
Green Valley	4.0	2.0	9.0	4.56 ± 0.2
Concord	4.3	3.1	9.0	3.47 ± 0.1
Calaveras (North)	6.0	3.0	7.0	4.65 ± 0.6
Calaveras (Central)	15.0	9.0	19.0	9.63 ± 0.9
Calaveras (South)	15.0	10.0	20.0	14.05 ± 1.1
Calaveras (South)–Paicines extension	10.0	5.0	15.0	8.60 ± 1.0

between the geologic preferred rates (black) and the combined geodetic and geologic inverted rate (red). Areas between the upper (green) and lower (red) geologic bounds are shaded in gray. In comparison to the UCERF3.1 geologic slip-rate data and the geologic bound data, the inverted slip rates from Santa Cruz all the way to the North Coast and offshore segments of the San Andreas fault zone agree well with the geologic estimates (Table 1). Inverted slip rates also agree well with the geologic preferred rates along the Maacama–Rodgers Creek–Hayward fault system (Table 2) and the Bartlett Springs–Green Valley–Calaveras fault segments (Table 3) in the north. Slip rates along the Bartlett Springs fault are 4–5 mm/yr above the preferred geologic rates. Given the large uncertainty for the geologic rates along the Bartlett Springs, those inverted rates lies well within the UCERF3.1 geologic bounds. A total of 40 mm/yr is accommodated by the northern San Andreas fault zone, Maacama–Rodgers Creek–Hayward fault system, and Bartlett Springs–Green Valley–Calaveras faults, matching well with the regional tectonic rates.

In southern California, our investigation has significantly improved agreement between inverted rates and geologic rates along the central and eastern Garlock fault (Table 4) in comparison with the previous block-model studies (e.g., McCaffrey, 2005; Meade and Hager, 2005). This provides an alternative explanation to the viscoelastic relaxation model of Chuang and Johnson (2011) on the Garlock faulting processes, although our inverted slip rate along the western Garlock fault is also significantly lower than that of the geologic lower bound. Modeled slip rates along the Coachella Valley and Brawley segment of the San Andreas fault zone (Table 1) and along the San Jacinto fault (Table 5) agree with their corresponding geologic rates. We also note that the rate along the Coachella Valley and Brawley segments is nearly twice the rate along the same San Jacinto fault branch (Table 5).

Although the two sets of slip rates agree with each other overall, the fault-based inversion model has significantly lower slip rates along the San Andreas fault zone from the Cholame segment through the Mojave to the northern San Bernardino Mountain segments in comparison with the UCERF3.1 geologic lower bound (Dawson and Weldon, 2013). Assuming that geologic slip rates represent long-term averages of many cycles of periods of high and low seismic

Table 4
Slip Rates along the Garlock Fault Using the Fault-Based Model

Fault Name	Geologic Slip Rate (mm/yr)	Lower Bound (mm/yr)	Upper Bound (mm/yr)	Inverted Slip Rate ± Error (mm/yr)
Garlock (West)	6.0	5.0	11.0	1.68 ± 0.7
Garlock (Central)	7.0	5.0	9.0	7.52 ± 0.7
Garlock (East)	3.0	1.0	5.0	4.87 ± 1.3

Table 5
Slip Rates along the San Jacinto Fault Using the Fault-Based Model

Fault Name	Geologic Slip Rate (mm/yr)	Lower Bound (mm/yr)	Upper Bound (mm/yr)	Inverted Slip Rate ± Error (mm/yr)
San Jacinto (San Bernardino)	8.0	2.0	12.0	13.12 ± 1.0
San Jacinto (San Jacinto Valley)	14.0	11.0	18.0	14.86 ± 1.0
San Jacinto (stepovers combined)	14.0	11.0	18.0	14.86 ± 1.0
San Jacinto (Anza)	14.0	11.0	18.0	12.89 ± 1.0
San Jacinto (Coyote Creek)	7.0	3.0	9.0	6.52 ± 0.8
San Jacinto (Clark)	8.0	6.0	11.0	6.19 ± 0.2
San Jacinto (Borrego)	5.0	1.0	10.0	8.56 ± 0.3
San Jacinto (Superstition Mountain)	6.0	2.0	8.0	9.47 ± 0.4

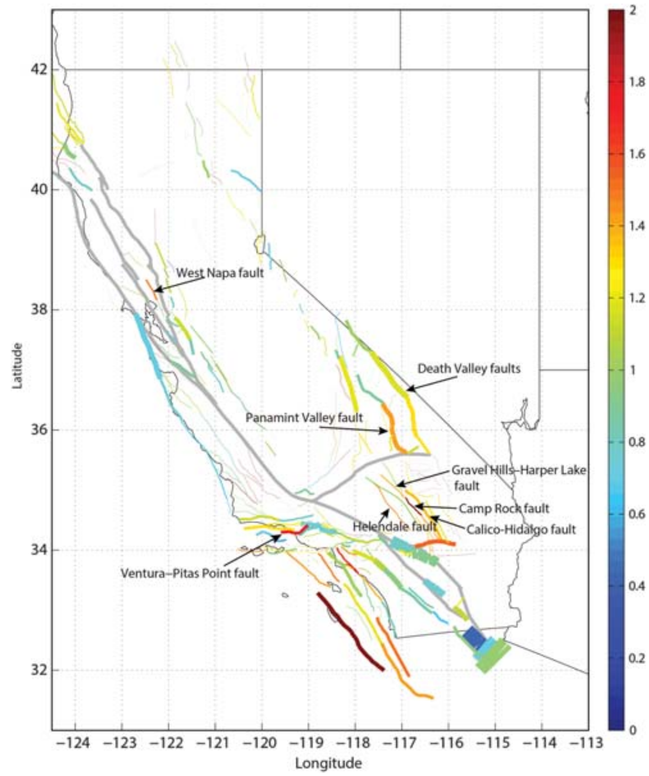

Figure 13. Map of ratios between geodetic rate and geologic rates. The line width is proportional to the geodetic rate.

activity along any given fault, our fault-based model estimates suggest these sections of the San Andreas system are currently experiencing a slow tectonic loading period. Meade and Hager (2005) and McCaffrey (2005) report similar low slip rates. Such slow deformation rates could be explained by a viscoelastic deformation model that takes into account temporal deformation within earthquake cycles (e.g., Chuang and Johnson, 2011; Hearn *et al.*, 2013; Smith-Konter *et al.*, 2014). Although these sections of the San Andreas fault zone are undergoing a slower period of tectonic loading, a significant increase in inverted slip rates is found on faults along the eastern California shear zone (i.e., along the Gravel Hills–Harper Lake and Camp Rock fault system, Calico–Hidalgo, and Helendale faults) to the southern Walker Lane (i.e., the Panamint Valley fault and Death Valley faults; Fig. 13 and Table 6) in comparison with the geologic estimates in the UCERF3 long-term geologic rate data, suggesting the region is experiencing a period of faster-than-average tectonic loading. With the Big Bend along the San Andreas fault zone as a barrier for the relative motion between the Pacific and North American plates, there is a gradual transfer in regional faulting activity from the San Andreas fault system to the eastern California shear zone and the Walker Lane (Nur *et al.*, 1993; Sleep and Fujita, 1997). As a consequence of two fault systems accommodating the same plate-boundary motion, there might be alternating periods of seismic activity between them (Dolan *et al.*, 2007). Alternatively, the lower slip rate along this portion of the San Andreas could be a result of a significant portion of the deformation occurring off the faults (Johnson, 2013; Herbert *et al.*, 2014).

For the type B faults in northern California and the Great Valley thrust system, our inverted slip rates fit within ±15% of the geologic preferred rates except for the West Napa fault (Fig. 13). Our estimated rate for West Napa is at 1.5 ± 0.7 mm/yr, about 50% higher than the geologic preferred rate. The occurrence of the M 6.0 West Napa earthquake (Brocher *et al.*, 2015) in 2014 may support the higher loading rate on West Napa found in this study.

Within the western Transverse Ranges, there is a series of thrust faults: the Cucamonga, Raymond, and Santa Monica faults in the south; the Oak Ridge, Santa Susana, San Cayetano, Mission Ridge, and Big Pine faults in the north; and bounded by the Sierra Madre and San Gabriel faults to the east. Slip rates for those faults are listed in Table 6. These faults accommodate up to 6 mm/yr of the preferred shortening motion. For most of these faults, the inverted slip rates agree reasonably well with the geologic preferred rates; the exception is the Ventura–Pitas Point fault, where inverted slip rate is nearly twice the preferred geologic rate (Fig. 13). For the San Cayetano fault, our inverted slip rate of 4.6 mm/yr is slightly less than the preferred geologic rate of 6 mm/yr. With an east–west-trending thrust, this fault

Table 6
Slip Rates along Other Significant B Faults Using the Fault-Based Model

Fault Name	Geologic Slip Rate (mm/yr)	Lower Bound (mm/yr)	Upper Bound (mm/yr)	Rake (°)	Inverted Slip Rate ± Error (mm/yr)	Rake (°)
Almanor	2.20	0.50	5.00	−135	2.25 ± 0.70	−136
Antelope Valley	1.00	0.50	1.50	−90	0.97 ± 0.34	−109
Big Lagoon–Bald Mountain	1.00	0.50	1.20	90	1.15 ± 0.27	71
Blackwater	0.50	0.20	1.00	180	0.52 ± 0.26	−161
Calico–Hidalgo	1.80	1.00	2.60	180	2.45 ± 0.27	−161
Camp Rock	0.60	0.20	2.00	180	1.20 ± 0.32	163
Carson Range (Genoa)	2.00	1.00	3.00	−90	1.45 ± 0.10	−90
Channel Islands thrust	1.50	0.50	2.00	90	1.41 ± 0.39	71
Chino	1.00	0.20	2.00	150	1.03 ± 0.40	161
Cleghorn	0.45	0.30	0.60	0	0.52 ± 0.29	19
Compton	0.90	0.30	1.40	90	1.19 ± 0.24	74
Coronado Bank	1.83	1.00	5.00	180	2.77 ± 0.45	−163
Cucamonga	1.50	1.00	2.00	90	1.64 ± 0.32	71
Death Valley (Black Mountains Frontal)	3.00	1.00	5.00	−150	3.86 ± 0.54	−144
Death Valley (Fish Lake Valley)	3.00	2.00	4.00	−150	3.07 ± 0.18	−157
Death Valley (North)	4.50	3.00	6.00	180	5.24 ± 0.40	−176
Death Valley (South)	1.83	1.00	5.00	180	2.35 ± 0.46	−161
Deep Springs	1.20	0.50	2.00	−90	1.24 ± 0.34	−109
Earthquake Valley	2.00	1.00	3.00	180	1.67 ± 0.30	175
Earthquake Valley (north extension)	2.00	1.00	3.00	180	1.62 ± 0.40	−177
Earthquake Valley (south extension)	2.00	1.00	3.00	180	1.65 ± 0.40	174
Elmore Ranch	1.00	0.50	1.50	0	1.23 ± 0.22	6
Elsinore (Coyote Mountains)	3.00	1.00	5.00	180	1.91 ± 0.34	−161
Elsinore (Glen Ivy)	5.00	3.00	7.00	180	5.38 ± 0.10	177
Elsinore (Julian)	3.00	1.00	5.00	180	2.61 ± 0.44	162
Elsinore (stepovers combined)	5.00	3.00	7.00	180	4.53 ± 0.31	−172
Elsinore (Temecula)	5.00	3.00	7.00	180	4.83 ± 0.14	−171
Elysian Park (upper)	1.90	0.80	2.20	90	1.83 ± 0.43	71
Fickle Hill (alt1)	0.60	0.20	1.20	90	0.70 ± 0.37	72
Garberville–Briceland	2.60	0.20	5.00	180	2.08 ± 0.57	161
Gravel Hills–Harper Lake	0.70	0.30	1.10	180	0.97 ± 0.32	163
Great Valley 03a Dunnigan Hills*	0.60	0.20	1.00	90	0.20 ± 0.10	90
Great Valley 03*	1.30	0.50	2.00	90	1.45 ± 0.40	108
Great Valley 04a Trout Creek*	1.30	0.50	2.00	90	1.28 ± 0.43	109
Great Valley 04b Gordon Valley*	1.30	0.50	2.00	90	1.38 ± 0.43	109
Great Valley 05*	1.80	0.50	3.00	180	1.48 ± 0.52	170
Great Valley 07*	0.90	0.80	1.20	90	0.89 ± 0.19	104
Great Valley 08*	0.50	0.40	0.60	90	0.53 ± 0.29	109
Great Valley 09*	1.70	1.40	2.30	90	1.74 ± 0.32	109
Great Valley 10*	1.00	0.50	1.50	90	1.01 ± 0.35	109
Great Valley 11*	1.00	0.50	1.50	90	0.93 ± 0.35	109
Great Valley 12*	1.00	0.50	1.50	90	0.93 ± 0.27	79
Great Valley 13*	1.00	0.50	1.50	90	0.84 ± 0.34	109
Great Valley 14*	1.00	0.50	1.50	90	0.96 ± 0.37	109
Greenville (North)	3.00	1.00	5.00	180	3.46 ± 0.30	−179
Greenville (South)	3.00	1.00	5.00	180	2.52 ± 0.41	−171
Hartley Springs	0.50	0.20	1.00	−90	0.61 ± 0.33	−109
Hat Creek–McArthur–Mayfield	0.60	0.20	1.00	−90	0.59 ± 0.26	−109
Helendale–South Lockhart	0.60	0.20	1.00	180	0.87 ± 0.16	171
Hilton Creek	1.50	1.00	2.00	−90	1.50 ± 0.33	−109
Hollywood	0.90	0.30	1.50	30	0.97 ± 0.30	29
Honey Lake	2.50	1.00	5.00	180	1.79 ± 0.25	−169
Hosgri	1.50	1.00	5.00	180	1.02 ± 0.29	−161
Hosgri (Extension)	0.60	0.20	3.00	180	0.39 ± 0.39	−161
Hunter Mountain–Saline Valley	3.00	1.00	5.00	−150	2.64 ± 0.23	−160
Kickapoo	0.60	0.20	1.00	180	0.65 ± 0.32	−161
Laguna Salada	3.00	1.00	5.00	180	2.85 ± 0.71	−161
Lenwood–Lockhart–Old Woman Springs	1.00	0.60	1.40	180	1.02 ± 0.26	−162
Little Lake	0.60	0.50	1.00	180	0.78 ± 0.27	−161
Little Salmon (offshore)	1.10	0.20	2.00	90	1.25 ± 0.46	71

(*continued*)

Table 6 (*Continued*)

Fault Name	Geologic Slip Rate (mm/yr)	Lower Bound (mm/yr)	Upper Bound (mm/yr)	Rake (°)	Inverted Slip Rate ± Error (mm/yr)	Rake (°)
Little Salmon (onshore)	4.50	2.00	8.00	90	4.26 ± 0.22	84
Lost Hills	0.90	0.20	1.50	90	0.93 ± 0.41	109
Mad River (alt1)	0.70	0.50	1.00	90	0.92 ± 0.34	71
McKinleyville (alt1)	0.60	0.20	0.80	90	0.66 ± 0.33	72
Mission (connected)	1.80	0.50	3.00	180	1.32 ± 0.56	161
Mission Creek	1.09	0.50	3.00	180	0.83 ± 0.41	161
Mission Hills	1.25	0.50	3.00	90	1.05 ± 0.36	72
Mission Ridge–Arroyo Parida–Santa Ana	0.90	0.40	1.60	90	1.11 ± 0.35	71
Mono Lake	0.90	0.30	1.50	−90	0.72 ± 0.32	−109
Monte Vista–Shannon	0.60	0.20	1.00	90	0.57 ± 0.34	108
Mount Diablo Thrust North	2.00	1.00	3.00	90	1.69 ± 0.47	106
Mount Diablo Thrust South	2.00	1.00	3.00	90	1.63 ± 0.43	101
Newport–Inglewood (offshore)	1.00	0.50	3.00	180	1.39 ± 0.35	−165
Newport–Inglewood alt1	1.00	0.50	3.00	180	1.63 ± 0.37	164
Northridge	1.50	0.50	2.50	90	1.88 ± 0.47	108
Northridge Hills	1.30	0.30	2.30	90	1.49 ± 0.50	71
North Tahoe	0.50	0.20	1.00	−90	0.58 ± 0.20	−90
Oak Ridge (onshore)	4.00	2.00	6.00	90	3.14 ± 0.40	90
Oceanside alt1	1.00	0.00	1.10	90	0.88 ± 0.12	95
Ortigalita (North)	1.50	0.50	2.50	180	1.36 ± 0.40	180
Ortigalita (South)	1.50	0.50	2.50	180	1.21 ± 0.46	−161
Owens Valley	3.50	2.00	5.00	180	4.21 ± 0.40	−177
Owens Valley–Keough Hot Springs	3.00	1.00	5.00	−90	2.55 ± 0.50	−109
Owl Lake	2.00	1.00	3.00	0	2.27 ± 0.46	−16
Palos Verdes	3.00	2.00	5.00	180	3.05 ± 0.27	161
Panamint Valley	3.00	1.00	5.00	−150	4.27 ± 0.50	−125
Pinto Mountain	2.50	1.00	5.00	0	3.87 ± 0.40	−4
Pisgah–Bullion Mountain–Mesquite Lake	1.00	0.20	1.20	180	1.19 ± 0.30	−162
Pitas Point (lower)–Montalvo	3.00	0.00	6.00	90	1.69 ± 0.60	90
Pitas Point (lower west)	3.00	0.00	6.00	90	2.22 ± 0.64	71
Pleito	2.00	0.50	3.00	90	1.80 ± 0.41	109
Puente Hills	0.90	0.20	1.50	90	1.28 ± 0.37	76
Raymond	2.00	1.00	5.00	60	1.39 ± 0.40	48
Red Mountain	2.00	1.00	5.00	90	2.61 ± 0.48	71
Robinson Creek	0.50	0.20	1.00	−90	0.61 ± 0.34	−71
Rose Canyon	2.00	1.00	5.00	180	1.73 ± 0.31	−162
Round Valley	0.60	0.20	1.00	−90	0.70 ± 0.33	−109
San Cayetano	6.00	3.00	9.00	90	4.61 ± 0.65	71
San Clemente	1.80	1.00	5.00	180	3.74 ± 0.60	171
San Diego trough north alt1	2.00	1.00	3.00	180	2.43 ± 0.31	−162
San Diego trough south	2.00	1.00	3.00	180	2.85 ± 0.43	−163
San Gorgonio Pass	1.80	0.50	3.00	90	2.23 ± 0.56	74
San Gregorio (North)	7.00	4.00	10.00	180	4.97 ± 0.20	179
San Gregorio (South)	3.00	2.00	6.00	180	2.28 ± 0.41	171
San Jacinto (Clark) rev	8.00	6.00	11.00	180	6.22 ± 0.22	174
San Jacinto (Lytle Creek connector)	2.50	1.00	5.00	180	2.19 ± 1.00	177
San Joaquin Hills	0.60	0.20	1.00	90	0.65 ± 0.37	109
San Pedro basin	1.00	0.00	2.00	180	1.47 ± 0.44	165
Santa Cruz Catalina ridge alt1	1.00	0.00	2.00	135	1.44 ± 0.20	116
Santa Cruz Island	0.60	0.20	1.00	30	0.79 ± 0.10	15
Santa Monica alt1	1.00	0.50	2.00	30	1.03 ± 0.38	29
Santa Rosa Island	0.60	0.20	1.50	30	0.87 ± 0.30	17
Santa Susana alt1	6.00	0.50	10.00	30	4.29 ± 0.47	36
Santa Susana East (connector)	6.00	0.50	10.00	90	4.13 ± 0.41	73
Santa Ynez (East)	2.00	0.20	3.00	0	1.61 ± 0.38	−18
Santa Ynez (West)	2.00	0.20	3.00	0	2.26 ± 0.38	−18
Sargent	3.00	1.00	5.00	180	2.65 ± 0.72	162
Sierra Madre	2.00	1.00	3.00	90	2.24 ± 0.41	71
Sierra Madre (San Fernando)	2.00	1.00	3.00	90	1.79 ± 0.50	71
Simi−Santa Rosa	0.60	0.20	1.00	30	0.66 ± 0.20	31
Superstition Hills	4.00	2.00	6.00	180	4.49 ± 0.71	167
Surprise Valley	0.70	0.20	1.00	−90	0.83 ± 0.29	−109

(*continued*)

Table 6 (*Continued*)

Fault Name	Geologic Slip Rate (mm/yr)	Lower Bound (mm/yr)	Upper Bound (mm/yr)	Rake (°)	Inverted Slip Rate ± Error (mm/yr)	Rake (°)
Table Bluff	0.60	0.20	1.00	90	0.75 ± 0.32	71
Tank Canyon	1.00	0.50	1.50	−90	1.21 ± 0.37	−109
Trinidad (alt1)	1.50	1.00	2.00	90	1.81 ± 0.35	71
Ventura–Pitas Point	1.60	0.50	10.00	60	2.84 ± 0.70	34
West Napa	1.00	0.20	5.00	180	1.50 ± 0.72	−162
West Tahoe	0.60	0.20	1.00	−90	0.75 ± 0.30	−109
White Mountains	0.60	0.20	1.00	180	0.39 ± 0.10	−161
Whittier alt1	3.00	1.00	5.00	150	3.51 ± 0.36	137

*Details of those Great Valley Faults are provided in Dawson (2013).

is capable of producing magnitude 7 and larger earthquakes and poses significant seismic hazard to the region (Petersen and Wesnousky, 1994; Dolan and Rockwell, 2001). The influence of the imposed overall minimization on the fault-normal slip-rate estimates over this fault was found to be insignificant within a 2% difference level. Shortening along the Big Pine, Cucamonga, Santa Susana, San Cayetano, and Mission Ridge faults also decreases from east to west, in agreement with the counterclockwise rotation in the area. Significant shortening is also found across the Puente Hills and Whittier thrust faults. Our inverted slip rate along the Puente Hills thrust fault is about 40% higher than the geologic preferred rate at 1.3 ± 0.4 mm/yr. Compared to the strike-slip motion, dip-slip motion is merely a second-order tectonic motion in southern California. However, the contribution of dip-slip motion is very important in seismic hazard and risk. Recent earthquakes (e.g., 1971 M_w 6.6 San Fernando, the 1987 M_w 5.9 Whittier Narrows, and the 1994 M_w 6.7 Northridge events) demonstrate that blind thrusts in the Los Angeles basin and the Transverse Range region can result in major damage to the region. Together, they pose significant seismic-hazard risk for the metropolitan population.

For most other major strike-slip type B faults in southern California, our inverted slip rates agree reasonably well with the geologic rates (i.e., Elsinore, Rose Canyon, and Palos Verdes). However, our inverted slip rate of 1.6 ± 0.4 mm/yr for the Newport–Inglewood fault is 60% higher than the geologic preferred rate. This right-lateral strike-slip fault system includes an onshore and an offshore section and is capable of producing magnitude 6–7.4 earthquakes (Petersen *et al.*, 1996). Our fault-based modeling study suggests higher seismic hazard in the greater Los Angeles Metropolitan area than that of the preferred geologic estimates.

For the off-coast faults in central California, modeled slip rates are within the geologic bounds but are about 20% less than the UCERF3-preferred geologic rates and near the lower bound for fault segments along the San Gregorio and Hosgri faults. For the off-shore faults in southern California, inverted slip rates are generally higher than the preferred geologic rates; for example, the rate along the San Clemente fault is twice that of the geologic preferred rates. Inverted slip rates are also 30% higher on the Red Mountain fault and more than 50% higher along the Santa Rosa Island, Santa Cruz–Catalina ridge, San Pedro basin, San Diego trough, and Coronado Bank faults compared with the geologic preferred rates. However, geologic slip rates along those offshore faults are not well constrained. Our inversion should help to constrain those slip rates and thereby improve seismic-hazard assessment along the California coast.

Off-Fault Deformation

Figure 14 plots the off-fault strain-rate distribution for (a) maximum strain rate and (b) maximum shear strain rate. Our maximum strain rate is defined as the largest of the two principal strain rates, dilatation rate and shear strain rate. Our off-fault strain rates are obtained based on the same block-model geometry (Fig. 2) without the type B faults, given the preferred slip-rate distribution along the boundaries of blocks. The model assumes buried dislocation sources below the locking depth. By allowing those sources to rupture up to the surface along the boundaries of the six major blocks, we simulate strain-rate tensors on a gridded $0.1° \times 0.1°$ surface covering California; we assume the same slip-rate distribution along their surface fault segments as that along their buried dislocation sources. Both maximum and shear off-fault strain-rate maps show fast straining regions along the North Coast segment of the San Andreas fault zone and Cascadia subduction zone in northern California. In southern California, high off-fault strain rates are distributed across the Transverse Ranges and along the Garlock fault zone and to the south along the Coachella and Brawley fault zones, continuing farther south across the border. The Sierra Nevada block appears more rigid, with a lower strain rate at a few nanostrains per year. We convert off-fault strain rates to moment rates within each gridded cell using the Kostrov (1974) formula following Savage and Simpson (1997), assuming a shear modulus of 3×10^{10} Pa and a seismogenic thickness of 11 km. The total on-fault moment rate from our preferred model is about 1.88×10^{19} N·m/yr, which is a 9% increase from the UCERF2 model. Our final off-fault strain-rate model gives a total off-fault moment rate of 0.88×10^{19} N·m/yr, which is about 32% of the total moment rate. The total moment rate is 2.76×10^{19} N·m/yr, which represents a 16% increase from the UCERF2 model. However, not all the increases are seismic, so the seismic/

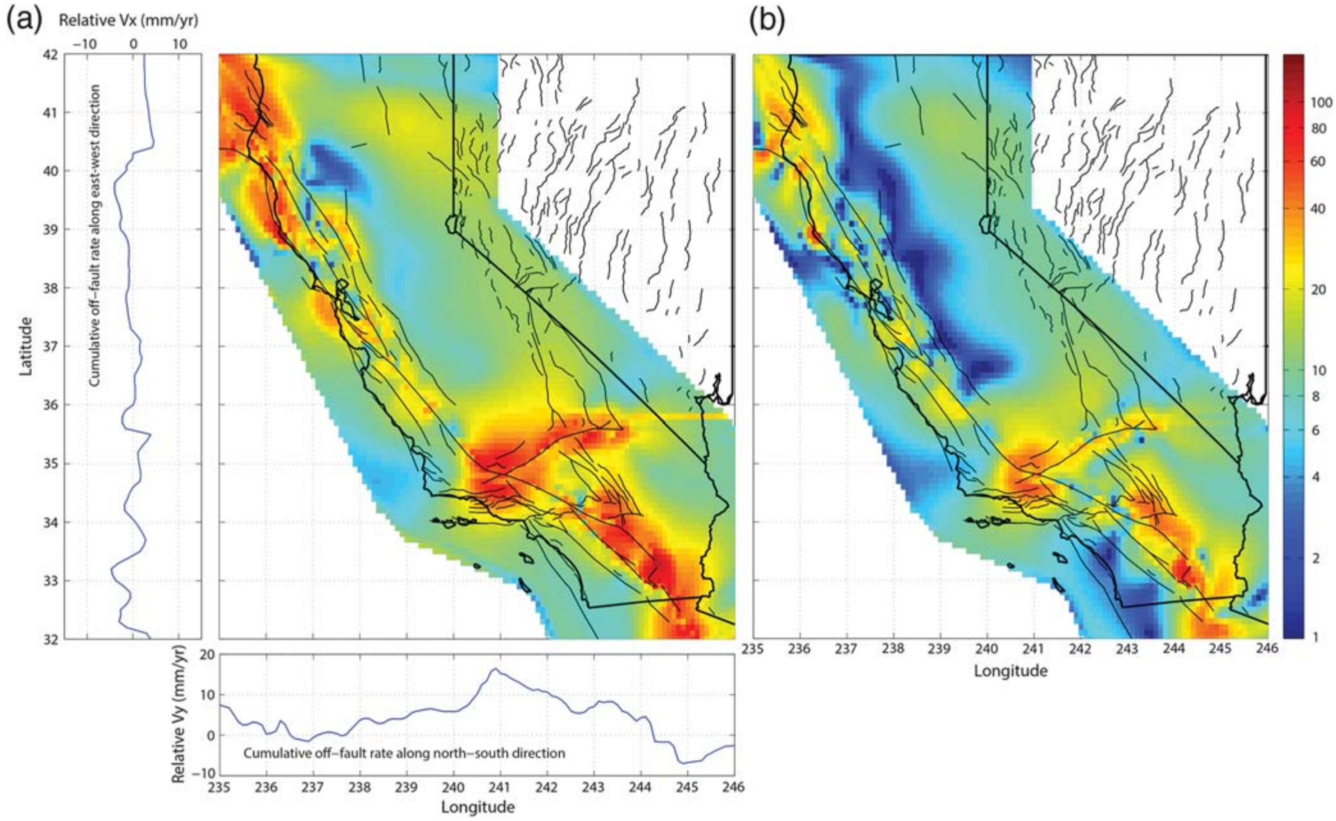

Figure 14. (a) Map of maximum off-fault strain-rate distribution in California. The left panel shows the cumulative east component off-fault-slip rate as a function of latitude and the bottom panel shows the cumulative north component off-fault slip rate as a function of longitude. Maximum strain rate is defined as the largest of the maximum principal strain rate, minimum principal strain rate, dilatation rate and shear strain rate. (b) Same as (a) but for the off-fault shear strain-rate distribution. Units in the color bar are nano-strains per year.

aseismic slip-rate ratios are critical for future seismic-hazard assessments.

Another way to quantify the off-fault deformation is to calculate the cumulative slip rate from the off-fault strain-rate distribution. This cumulative slip rate across the region can be estimated using

$$v_x(x_2) - v_x(x_1) = \int_{x_1}^{x_2} \frac{\partial v_x}{\partial x} dx = \int_{x_1}^{x_2} \dot{e}_{xx} dx \qquad (2)$$

and

$$v_y(y_2) - v_y(y_1) = \int_{y_1}^{y_2} \frac{\partial v_y}{\partial y} dy = \int_{y_1}^{y_2} \dot{e}_{yy} dy, \qquad (3)$$

in which v_x and v_y are east and north velocity components; x_1 and x_2 are longitudes along west and east boundaries of the gridded zone (Fig. 14) as a function of latitude, respectively; and y_1 and y_2 are latitudes along south and north boundaries as a function of longitude, respectively. Variables $e^{\cdot}_{xx}$ and $e^{\cdot}_{yy}$ are components of horizontal strain-rate tensors. The left panel of Figure 14a is a plot of the cumulative east component off-fault-slip rate as a function of latitude, and the bottom panel is a plot of the cumulative north component off-fault slip rate as a function of longitude. Apparently the cumulative east component off-fault rate fluctuates around ± 4 mm/yr. The cumulative north component off-fault rate peaks at 241° in longitude at 18 mm/yr across the Transverse Range and Big Bend area.

Figure 15 shows comparisons of the on-fault cumulative geologic slip rates and our combined-inversion slip rates along east–west-oriented profiles located at 0.1° intervals from 32° to 42° latitude for north (Fig. 15a) and east (Fig. 15b) component motions. Deformation model transects are calculated by finding the east and north components of slip on each model fault, using the input geometry (strike, dip, dip-direction) and output slip rates and rakes. East and north components are summed along transects, and the implied motion vectors (magnitude and direction) are calculated. The off-fault deformation is not included in the transects so as to enable comparison with the UCERF3 geologic model. The transects show total cumulative slip rate up to 50 mm/yr for both east (Fig. 15a) and north components (Fig. 15b), with averages around 28 and 35 mm/yr for the east and north relative motions, respectively. The dashed lines are the relative motion between the North American and Pacific plates based on the NUVEL-1A model (DeMets *et al.*, 1994). In comparison with the reference NUVEL-1A model, we find significant deviations in north-component motion along 33.5–36 transects. Large off-fault deformation

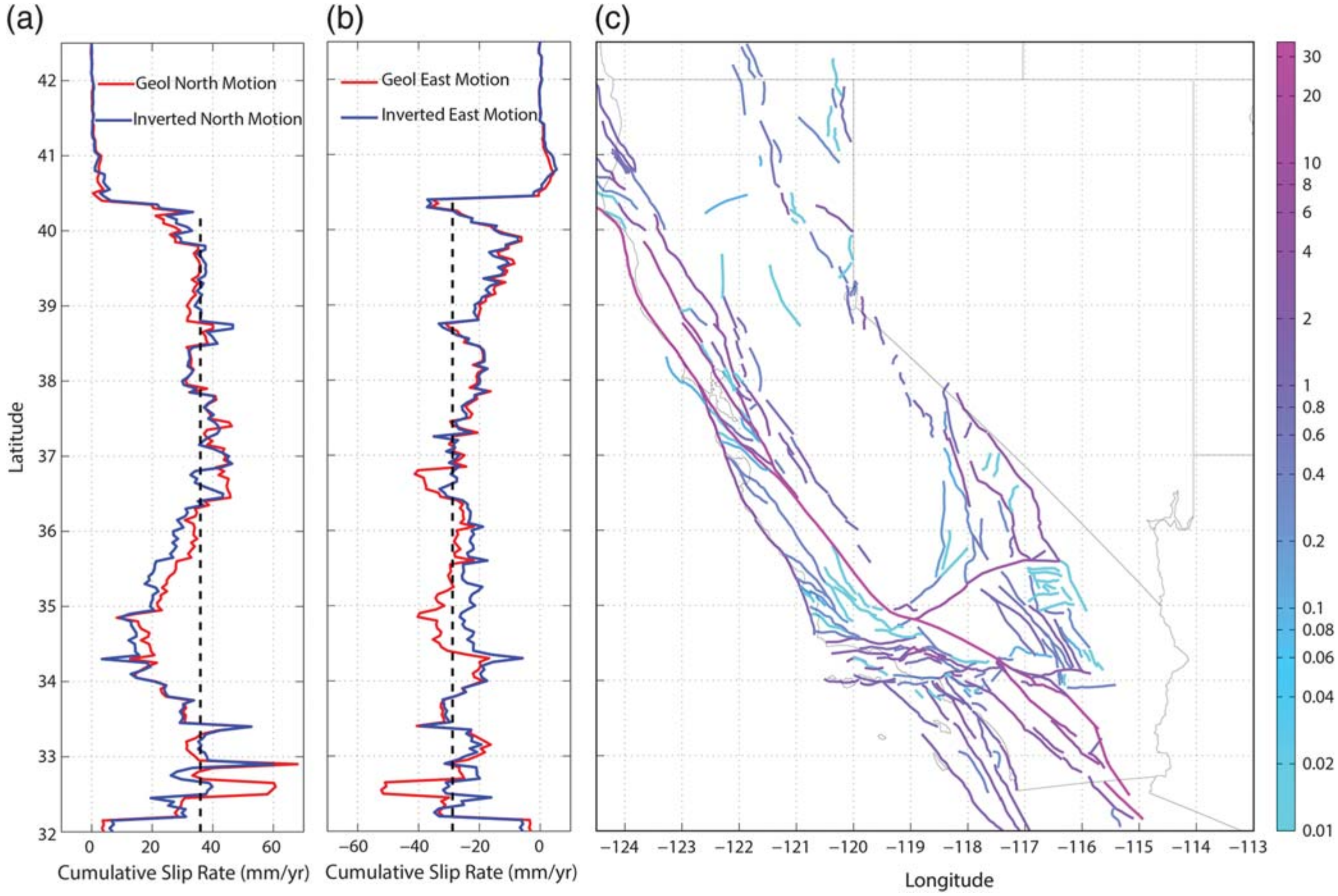

Figure 15. (a) The cumulative on-fault total slip rate along the geologic north motion direction summed along the east–west-oriented profiles for the UCERF3.1 geologic slip rates, and the preferred fault-based deformation model slip rates at 0.1° intervals from 32° to 42° latitude in reference to the North American plate. (b) Same as (a) but for the geologic east motion direction. Dashed lines represent the relative motion between the North American and the Pacific plates, based on the NUVEL-1A model (DeMets *et al.*, 1994). (c) Map of California fault traces colored based on the magnitude of the estimated fault slip rates from the preferred inversion model. Units in the color bar are millimeters per year.

(up to 18 mm/yr) occurs along the region (bottom panel in Fig. 14a). The sum of on-fault and off-fault north-component deformation along these transects adds 35 ± 5 mm/yr. Both models also deviate significantly from the NUVEL-1A model between 37.5° and 40° in east-component motion due to omitting the off-fault deformation along the northern off-coast San Andreas fault zone (Fig. 14a) and a significant oblique motion up to 10 mm/yr through northern Walker Lane between northern California and Nevada (Thatcher *et al.*, 1999). In general, the two rates track each other well.

Conclusion

Decades of dense GPS velocity observations are available in California and its near neighbors. Analysis of these geodetic signals provides fundamental data on present-day fault slip rates on major active faults, and these data provide critical input on earthquake occurrence that leads to better seismic-hazard assessment. We studied fault slip rates on major faults in California and in neighboring regions using a fault-based model of crustal deformation. Our model consists of six major blocks bounded by type A faults, with the type B faults distributed in the block interiors. Both GPS velocities and geologic slip-rate data are used to constrain our model. With the geologic input constraints, the fits to GPS observations were compromised with a normalized chi-square error of 15.1 and a mean velocity residual of 1.6 mm/yr, which is in the middle of other UCERF3 deformation models (Parsons *et al.*, 2013). In addition, our combined inversion was further constrained by the geologic bounds for all the California type B faults. The difference in terms of GPS data fitting between models with and without this additional constraint is less than 2%.

Our least-squares inversion shows that slip rates along major faults in northern California agree well with the UCERF3 geologic estimates within the geologic uncertainties; for example, along the northern San Andreas fault, the Maacama–Rodgers Creek–Hayward fault system, and the Bartlett Springs–Green Valley–Calaveras fault segments. The total slip rates across transects of those faults amount to 40 mm/yr, matching the tectonic rate for the region. Slip rates along the Bartlett Springs and Hunting Creek fault system are twice the preferred geologic rates but are still within the geologic bounds.

Slip rates determined for the central and eastern Garlock fault match closely with their geologic rates, although the rate for the western Garlock is significantly lower than the geologic estimates. For the Transverse Range faults, the inverted slip rates agree reasonably well with the geologic preferred rates except for the Ventura–Pitas Point fault, where the inverted slip rate is nearly twice the preferred geologic value. The inverted slip rates along the Puente Hills and Whittier thrust faults are significantly higher than the geologic rates, suggesting higher urban seismic hazard than previously estimated.

Along the central and southern San Andreas fault zone from the creeping section to the San Bernardino Mountain segments, our fault-based model shows a significant decrease of 7–16 mm/yr in slip-rate estimates in comparison with the UCERF3-preferred geologic rate. In particular, along the Mojave and northern San Bernardino segments, the inverted rates are $20.0–22.0 \pm 0.7$ and 8.4 ± 0.7 mm/yr in comparison with geologic rates of 32.5 and 24 mm/yr, respectively. Along the eastern California shear zone and southern Walker Lane, the inverse model indicates a cumulative increase of $\sim$1 mm/yr in slip rates across the region in comparison with the geologic model. This suggests a decreased seismic hazard around the southern San Andreas fault zone and an increased seismic hazard along the eastern California and southern Walker Lane regions in relation to the model used in the USGS 2008 seismic-hazard assessment (Petersen *et al.*, 2008).

For the central off-coast faults along the San Gregorio and Hosgri, slip rates are 20% lower than their preferred geologic rates and are close to their geologic lower bounds. For the southern off-coast faults, slip rates are much higher than their preferred geologic rates and are close to their geologic upper bounds; in some cases, for example, rates are more than 50% higher along the San Clemente, Santa Cruz–Catalina Ridge, San Diego trough, and Coronado Bank faults in comparison with their geologic preferred estimates. In general, off-coast slip rates are not well constrained. Our inversion estimates should provide critical inputs and improve the seismic-hazard assessment along the California coast.

For the off-fault strain rates, fast-straining regions are found along the offshore and North Coast San Andreas and the southern Cascadia subduction zone. Large off-fault straining zones also occur across the Transverse Ranges and Garlock fault zone. Large off-fault strain rates continue from Landers to Brawley and then extend farther south across the border. By converting from strain rate to seismic moment rate, we find a total off-fault moment rate of 0.88×10^{19} N·m/yr. This total off-fault moment rate is about 32% of the total moment rate in the region. The total on-fault and off-fault moment rate is 2.76×10^{19} N·m/yr, which is a 16% increase from the UCERF2 model. Our preferred combined inversion model was applied to the UCERF3 fault-slip rate model with 30% weight (Field *et al.*, 2014).

Data and Resources

Downloadable files for the Uniform California Earthquake Rupture Forecast Version 3 (UCERF3) faults and deformation models are available at wgcep.org/components-deformation_model_3x (last accessed April 2014). Downloadable files for the USGS Quaternary Fault and Fold Database of the United States are available at http://earthquake.usgs.gov/hazards/qfaults (last accessed January 2016). Global Positioning System (GPS) velocity data were provided by Tom Herring at Massachusetts Institute of Technology under the UNAVCO western United States GPS velocity project.

Acknowledgments

This work has been supported by the Southern California Earthquake Center (SCEC) Uniform California Earthquake Rupture Forecast Version 3 (UCERF3) project and the U.S. Geological Survey (USGS Grant G11AP20044). We are grateful for many critical reviews from the SCEC UCERF3 Scientific Review Panel. We also thank Tom Parsons, Wayne Thatcher, Kaj Johnson, Kathy Haller, Mark Petersen, Jill McCarthy, Janet Slate, and two anonymous reviewers for many constructive comments and suggestions.

References

Banerjee, P., F. Pollitz, and R. Bürgmann (2005). The size and duration of the Sumatra–Andaman earthquake from far-field static offsets, *Science* **308,** 1769–1772, doi: 10.1126/science.1113746.

Bird, P. (2009). Long-term fault slip rates, distributed deformation rates, and forecast of seismicity in the western United States from joint fitting of community geologic, geodetic, and stress-direction datasets, *J. Geophys. Res.* **114,** no. B11403, doi: 10.1029/2009JB006317.

Brocher, T. M., A. S. Baltay, J. L. Hardebeck, F. F. Pollitz, J. R. Murray, A. L. Llenos, D. P. Schwartz, J. L. Blair, D. J. Ponti, and J. J. Lienkaemper (2015). The M_w 6.0 24 August 2014 South Napa earthquake, *Seismol. Res. Lett.* **86,** 309–326, doi: 10.1785/0220150004.

Chuang, R. Y., and K. M. Johnson (2011). Reconciling geologic and geodetic model fault slip-rate discrepancies in southern California—Consideration of nonsteady mantle flow and lower crustal fault creep, *Geology* **39,** no. 7, 627–630.

d'Alessio, M. A., I. A. Johanson, R. Bürgmann, D. A. Schmidt, and M. H. Murray (2005). Slicing up the San Francisco Bay Area: Block kinematics and fault slip rates from GPS-derived surface velocities, *J. Geophys. Res.* **110,** doi: 10.1029/2004JB003496.

Dawson, T. E. (2013). Appendix A: Updates to the California reference fault parameter database: UCERF3 fault models 3.1 and 3.2, *U.S. Geol. Surv. Open-File Rept. 2013-1165-A and California Geol. Surv. Special Rept. 228-A*.

Dawson, T. E., and R. J. Weldon II (2013). Appendix B: Geologic slip-rate data and geologic deformation model, *U.S. Geol. Surv. Open-File Rept. 2013-1165-B, and California Geol. Surv. Special Rept. 228-B*.

DeMets, C., R. G. Gordon, D. F. Argus, and S. Stein (1994). Effect of recent revisions of the geomagnetic reversal time scale on estimate of current plate motions, *Geophys. Res. Lett.* **21,** no. 20, 2191–2194.

Dolan, J. F., and T. K. Rockwell (2001). Paleoseismologic evidence for a very large ($M_w > 7$), recent surface rupture on the eastern San Cayetano fault, Ventura County, California: Was this the source of the damaging December 21, 1812 earthquake? *Bull. Seismol. Soc. Am.* **91,** 1417–1432.

Dolan, J. F., D. D. Bowman, and C. G. Sammis (2007). Long-range and long-term fault interactions in southern California, *Geology* **35,** 855–858.

Field, E. H., R. J. Arrowsmith, G. P. Biasi, P. Bird, T. E. Dawson, K. R. Felzer, D. D. Jackson, K. M. Johnson, T. H. Jordan, C. Madden, *et al.* (2014). Uniform California Earthquake Rupture Forecast, Version 3

(UCERF3): The time independent model, *Bull. Seismol. Soc. Am.* **104,** 1122–1180, doi: 10.1785/0120130164.

Field, E. H., T. E. Dawson, K. R. Felzer, A. D. Frankel, V. Gupta, T. H. Jordan, T. Parsons, M. D. Petersen, R. S. Stein, R. J. Weldon, and C. J. Wills (2009). Uniform California earthquake rupture forecast, Version 2 (UCERF 2), *Bull. Seismol. Soc. Am.* **99,** no. 4, 2053–2107.

Hauksson, E. (2000). Crustal structure and seismicity distribution adjacent to the Pacific and North America plate boundary in southern California, *J. Geophys. Res.* **105,** 13,875–13,903.

Hearn, E. H., F. F. Pollitz, W. R. Thatcher, and C. T. Onishi (2013). How do "ghost transients" from past earthquakes affect GPS slip rate estimates on southern California faults? *Geochem. Geophys. Geosyst.* **14,** no. 4, 828–838, doi: 10.1002/ggge.20080.

Herbert, J. W., M. L. Cooke, M. Oskin, and O. Difo (2014). How much can off-fault deformation contribute to the slip rate discrepancy within the eastern California shear zone? *Geology* **42,** no. 1, 71–75, doi: 10.1130/G34738.1.

Hill, D. P., J. P. Eaton, and L. M. Jones (1990). Seismicity of the San Andreas fault system: 1980–1986, in *The San Andreas Fault System*, R. E. Wallace (Editor), *U.S. Geol. Surv. Profess. Pap. 1515*, 115–152.

Johnson, K. M. (2013). Slip rates and off-fault deformation in southern California inferred from GPS data and models, *J. Geophys. Res.* **118,** no. 10, 5643–5664, doi: 10.1002/jgrb.50365.

Johnson, K. M., G. E. Hilley, and R. Burgmann (2007). Influence of lithosphere viscosity structure on estimates of fault slip rate in the Mojave region of the San Andreas fault system, *J. Geophys. Res.* **112,** no. B07408, doi: 10.1029/2006JB004842.

Kostrov, B. V. (1974). Seismic moment and energy of earthquakes, and seismic flow of rock, *Phys. Solid Earth* **1,** 23–44.

Liu, S., Z.-K. Shen, and R. Bürgmann (2015). Recovery of secular deformation field of Mojave shear zone in southern California from historical terrestrial and GPS measurements, *J. Geophys. Res.* **120,** 3965–3990, doi: 10.1002/2015JB011941.

McCaffrey, R. (2005). Block kinematics of the Pacific–North America plate boundary in the southwestern United States from inversion of GPS, seismological, and geologic data, *J. Geophys. Res.* **110,** no. B07401, doi: 10.1029/2004JB003307.

Meade, B. J., and B. H. Hager (2005). Block models of crustal motion in southern California constrained by GPS measurements, *J. Geophys. Res.* **110,** no. B03403, doi: 10.1029/2004JB003209.

Nur, A., H. Ron, and G. C. Beroza (1993). The nature of the Landers–Mojave earthquake line, *Science* **271,** no. 5118, 201–203.

Okada, Y. (1985). Surface deformation due to shear and tensile faults in a half-space, *Bull. Seismol. Soc. Am.* **75,** 1435–1154.

Parsons, T., K. M. Johnson, P. Bird, J. M. Bormann, T. E. Dawson, E. H. Field, W. C. Hammond, T. A. Herring, R. McCaffrey, Z.-K. Shen, *et al.* (2013). Appendix C: Deformation models for UCERF3.3, *U.S. Geol. Surv. Open-File Rept. 2013-1165-C, and California Geol. Surv. Special Rept. 228-C*.

Petersen, M. D., and S. G. Wesnousky (1994). Fault slip rates and earthquake histories for active faults in southern California, *Bull. Seismol. Soc. Am.* **84,** no. 5, 1608–1649.

Petersen, M. D., W. A. Bryant, C. H. Cramer, T. Cao, M. S. Reichle, A. D. Frankel, J. J. Lienkaemper, P. A. McCrory, and D. P. Schwartz (1996). Probabilistic seismic hazard assessment for the state of California, *California Division of Mines and Geology Open-File Rept. 96-08 and U.S. Geol. Surv. Open-File Rept. 96-706*.

Petersen, M. D., A. D. Frankel, S. C. Harmsen, C. S. Mueller, K. M. Haller, R. L. Wheeler, R. L. Wesson, Y. Zeng, O. S. Boyd, D. M. Perkins, *et al.* (2008). Documentation for the 2008 update of the United States National Seismic Hazard Maps, *U.S. Geol. Surv. Open-File Rept. 2008-1128*.

Petersen, M. D., M. P. Moschetti, P. M. Powers, C. S. Mueller, K. M. Haller, A. D. Frankel, Y. Zeng, S. Rezaeian, S. C. Harmsen, O. S. Boyd, *et al.* (2014). Documentation for the 2014 update of the United States national seismic hazard maps, *U.S. Geol. Surv. Open-File Rept. 2014-1091*, 243 pp., doi: 10.3133/ofr20141091.

Petersen, M. D., Y. Zeng, K. M. Haller, R. McCaffrey, W. C. Hammond, P. Bird, M. P. Moschetti, Z.-K. Shen, J. Bormann, and W. R. Thatcher (2013). Geodesy- and geology-based slip-rate models for the western United States (excluding California) national seismic hazard maps, *U.S. Geol. Surv. Open-File Rept. 2013-1293*, 80 pp., doi: 10.3133/ofr20131293.

Pollitz, F. F., and D. Schwartz (2008). Probabilistic seismic hazard in the San Francisco Bay area based on a simplified viscoelastic-cycle model of fault interactions, *J. Geophys. Res.* **113,** no. B05409, doi: 10.1029/2007JB005227.

Savage, J., and R. Burford (1973). Geodetic determination of relative plate motion in central California, *J. Geophys. Res.* **78,** 832–845.

Savage, J. C., and R. W. Simpson (1997). Surface strain accumulation and the seismic moment tensor, *Bull. Seismol. Soc. Am.* **87,** no. 5, 1345–1353.

Shen, Z.-K., R. W. King, T. A. Herring, and D. C. Agnew (2006). SCEC crustal motion map: Collaborative analysis report for 2006, *2006 SCEC Annual Technique Report*.

Sleep, N. J., and K. Fujita (1997). *Principles of Geophysics*, John Wiley and Sons, Chichester, West Sussex.

Smith-Konter, B. R., G. M. Thornton, and D. T. Sandwell (2014). Vertical crustal displacement due to interseismic deformation along the San Andreas fault: Constraints from tide gauges, *Geophys. Res. Lett.* **41,** doi: 10.1002/2014GL060091.

Sun, W., S. Okubo, G. Fu, and A. Araya (2009). General formulations of global co-seismic deformations caused by an arbitrary dislocation in a spherically symmetric earth model—Applicable to deformed earth surface and space-fixed point, *Geophys. J. Int.* **177,** 817–833, doi: 10.1111/j.1365-246X.2009.04113.x.

Thatcher, W., G. R. Foulger, B. R. Julian, J. Svarc, E. Quilty, and G. W. Bawden (1999). Present-day deformation across the Basin and Range province, western United States, *Science* **283,** 1714–1718.

Zeng, Y., and Z.-K. Shen (2014). Fault network modeling of crustal deformation in California constrained using GPS and geologic observations, *Tectonophysics* **612-613,** 1–14.

USGS Geologic Hazards Science Center
MS 966, Box 25046
Denver, Colorado 80225
zeng@usgs.gov
(Y.Z.)

Department of Earth and Space Sciences
University of California, Los Angeles
Los Angeles, California 90095-1567
(Z.-K.S.)

Manuscript received 7 January 2016;
Published Online 15 March 2016